The Astrophysical Journal, 842:24 (21pp), 2017 June 10 https://doi.org/10.3847/1538-4357/aa7414

Chemical Complexity in the Eu-enhanced Monometallic Globular NGC 5986*

Christian I. Johnson[1,7], Nelson Caldwell[1], R. Michael Rich[2], Mario Mateo[3], John I. Bailey III[4], Edward W. Olszewski[5], and Matthew G. Walker[6]

[1] Harvard-Smithsonian Center for Astrophysics, 60 Garden Street, MS-15, Cambridge, MA 02138, USA; cjohnson@cfa.harvard.edu, ncaldwell@cfa.harvard.edu
[2] Department of Physics and Astronomy, UCLA, 430 Portola Plaza, Box 951547, Los Angeles, CA 90095-1547, USA; rmr@astro.ucla.edu
[3] Department of Astronomy, University of Michigan, Ann Arbor, MI 48109, USA; mmateo@umich.edu
[4] Leiden Observatory, Leiden University, P.O. Box 9513, 2300RA Leiden, The Netherlands; baileyji@strw.leidenuniv.nl
[5] Steward Observatory, The University of Arizona, 933 N. Cherry Avenue, Tucson, AZ 85721, USA; eolszewski@as.arizona.edu
[6] McWilliams Center for Cosmology, Department of Physics, Carnegie Mellon University, 5000 Forbes Avenue, Pittsburgh, PA 15213, USA mgwalker@andrew.cmu.edu

Received 2017 March 13; revised 2017 May 10; accepted 2017 May 16; published 2017 June 8

Abstract

NGC 5986 is a poorly studied but relatively massive Galactic globular cluster that shares several physical and morphological characteristics with "iron-complex" clusters known to exhibit significant metallicity and heavy-element dispersions. In order to determine whether NGC 5986 joins the iron-complex cluster class, we investigated the chemical composition of 25 red giant branch and asymptotic giant branch cluster stars using high-resolution spectra obtained with the Magellan-M2FS instrument. Cluster membership was verified using a combination of radial velocity and [Fe/H] measurements, and we found the cluster to have a mean heliocentric radial velocity of $+99.76\,\mathrm{km\,s^{-1}}$ ($\sigma = 7.44\,\mathrm{km\,s^{-1}}$). We derived a mean metallicity of [Fe/H] $= -1.54$ dex ($\sigma = 0.08$ dex), but the cluster's small dispersion in [Fe/H] and low [La/Eu] abundance preclude it from being an iron-complex cluster. NGC 5986 has $\langle$[Eu/Fe]$\rangle = +0.76$ dex ($\sigma = 0.08$ dex), which is among the highest ratios detected in a Galactic cluster, but the small [Eu/Fe] dispersion is puzzling because such high values near [Fe/H] ~ -1.5 are typically only found in dwarf galaxies exhibiting large [Eu/Fe] variations. NGC 5986 exhibits classical globular cluster characteristics, such as uniformly enhanced [α/Fe] ratios, a small dispersion in Fe-peak abundances, and (anti) correlated light-element variations. Similar to NGC 2808, we find evidence that NGC 5986 may host at least four to five populations with distinct light-element compositions, and the presence of a clear Mg–Al anticorrelation along with an Al–Si correlation suggests that the cluster gas experienced processing at temperatures $\gtrsim$65–70 MK. However, the current data do not support burning temperatures exceeding $\sim$100 MK. We find some evidence that the first- and second-generation stars in NGC 5986 may be fully spatially mixed, which could indicate that the cluster has lost a significant fraction of its original mass.

Key words: globular clusters: general – globular clusters: individual (NGC 5986) – stars: abundances

1. Introduction

In contrast to the expectation that stars within a single globular cluster should exhibit relatively uniform composition patterns, early high-resolution spectroscopic analyses found that the abundances of elements such as O, Na, and Al can vary significantly between stars in the same cluster (e.g., Cohen 1978; Peterson 1980; Norris et al. 1981; Norris & Pilachowski 1985; Hatzes 1987). Subsequent observations confirmed these early results and expanded on the realization that not only are certain element pairs, such as O and Na, (anti) correlated (e.g., Drake et al. 1992; Kraft et al. 1993, 1997; Norris & Da Costa 1995; Pilachowski et al. 1996; Sneden et al. 1997, 2000; Ivans et al. 1999, 2001; Cavallo & Nagar 2000), but also similar light-element abundance patterns are present in nearly all old ($\gtrsim$6–8 Gyr) Galactic globular clusters (e.g., Carretta et al. 2009a, 2009b; see also reviews by Gratton et al. 2004, 2012a). Recently, the list has grown to include old extragalactic globular clusters as well (Mucciarelli et al. 2009; Schiavon et al. 2013; Larsen et al. 2014; Dalessandro et al. 2016; Niederhofer et al. 2017; Hollyhead et al. 2017), which supports the suggestion by Carretta et al. (2010b) that a population's stars must exhibit an O–Na anticorrelation to be labeled as a globular cluster.

Since the heavier α- and Fe-peak-element abundances typically exhibit small ($\lesssim$0.1 dex) star-to-star dispersions within globular clusters, the light-element (anti)correlations have been interpreted as a by-product of high-temperature (>40 MK) proton-capture burning (e.g., Denisenkov & Denisenkova 1990; Langer et al. 1993, 1997; Prantzos et al. 2007). Initial analyses of bright red giant branch (RGB) stars suggested that in situ processing and deep mixing could be responsible for a majority of the abundance variations (see, e.g., review by Kraft 1994). However, the discovery of similar chemical trends in globular cluster main-sequence and subgiant branch stars (e.g., Briley et al. 1994, 1996; Gratton et al. 2001; Cohen & Meléndez 2005; Bragaglia et al. 2010b; D'Orazi et al. 2010; Dobrovolskas et al. 2014) revealed that the chemical composition variations must be a result of pollution from a previous generation of more massive stars.

Interestingly, the introduction of *Hubble Space Telescope* (*HST*) optical and near-UV photometry to the field showed that globular clusters form distinct populations of stars with unique light-element compositions (e.g., Piotto et al. 2007, 2012, 2015; Milone et al. 2012a, 2012b) rather than the continuous distributions that are expected from simple dilution models. When combined with ground-based high-resolution spectroscopy, combinations of color and pseudo-color indices can be

* This paper includes data gathered with the 6.5 m Magellan Telescopes located at Las Campanas Observatory, Chile.
[7] Clay Fellow.

used to create "chromosome" maps (Milone et al. 2015a, 2015b) that anchor the photometry of different stellar populations to specific compositions. Furthermore, a combination of these chromosome maps, isochrone fitting, and direct measurements has shown that, as a consequence of proton-capture nucleosynthesis, stars with enhanced abundances of [N/Fe],[8] [Na/Fe], and [Al/Fe] and low abundances of [C/Fe], [O/Fe], and [Mg/Fe] are also enriched in He, with ΔY ranging from $\sim$0.01 to 0.15 (e.g., Norris 2004; Piotto et al. 2005; Bragaglia et al. 2010a, 2010b; Dupree et al. 2011; Pasquini et al. 2011; Milone et al. 2012b; Villanova et al. 2012; Milone 2015). In fact, the discrete nature of multiple populations in globular clusters, the variety of He enhancements and light-element patterns, and the large fraction ($\sim$60%–80%; Carretta 2015, their Figure 16) of polluted "second-generation" stars in clusters place strong constraints on the possible pollution sources and enrichment timescales. However, identifying and quantifying the exact pollution source(s) remain unsolved problems (see, e.g., critical discussions in Renzini 2008; Valcarce & Catelan 2011; Bastian & Lardo 2015; Bastian et al. 2015; Renzini et al. 2015; D'Antona et al. 2016).

As an added complication, a small but growing number of $\sim$10 "iron-complex" globular clusters are now known to possess intrinsic spreads in [Fe/H] that are found concurrent with the aforementioned light-element abundance variations (e.g., Marino et al. 2009, 2011a, 2011b, 2015; Carretta et al. 2010c, 2011; Johnson & Pilachowski 2010; Yong et al. 2014b; Johnson et al. 2015b, 2017).[9] These clusters are suspected to be the remnant cores of former dwarf spheroidal galaxies (e.g., Bekki & Freeman 2003; Lee et al. 2007; Georgiev et al. 2009; da Costa 2016) and therefore may trace a part of the Galaxy's minor merger history. Despite exhibiting broad ranges in mass, metallicity, and galactocentric distance, iron-complex clusters share several notable features: (1) they are among the most massive clusters in the Galaxy and all have $M_V < -8.3$; (2) most have very blue and extended horizontal branch morphologies; (3) the dispersion in [Fe/H] is $\gtrsim$0.1 dex when measured from high-resolution spectra; (4) several clusters contain discrete metallicity groups rather than just broadened distributions; (5) many have $\langle$[Fe/H]$\rangle \sim -1.7$; and (6) in all cases the stars with higher [Fe/H] have strong *s*-process enhancements. Using these characteristics as a template, we can search for new iron-complex clusters by measuring light- and heavy-element abundances in previously unobserved massive clusters with extended blue horizontal branches.

In this context, da Costa (2016) noted that NGC 5986 may be a promising iron-complex candidate. This cluster is relatively massive with $M_V = -8.44$ (Harris 1996; 2010 revision), has an irregular and highly eccentric prograde–retrograde orbit (Casetti-Dinescu et al. 2007; Allen et al. 2008; Moreno et al. 2014), hosts a predominantly blue and very extended horizontal branch (Kravtsov et al. 1997; Ortolani et al. 2000; Rosenberg et al. 2000; Alves et al. 2001; Momany et al. 2004; Piotto et al. 2015), and is estimated to have [Fe/H] ≈ -1.6 (Zinn & West 1984; Geisler et al. 1997; Ortolani et al. 2000; Kraft & Ivans 2003; Jasniewicz et al. 2004; Rakos & Schombert 2005; Dotter et al. 2010). However, except for an investigation into the composition of two post-asymptotic giant branch (AGB) stars by Jasniewicz et al. (2004), no detailed chemical abundance analysis has been performed for NGC 5986. Therefore, we present here a detailed composition analysis of 25 RGB and AGB stars in NGC 5986 and aim to determine whether the cluster belongs to the iron-complex class or is instead a more typical monometallic cluster.

2. Observations and Data Reduction

The spectra for this project were acquired using the Michigan–Magellan Fiber System (M2FS; Mateo et al. 2012) and MSpec spectrograph mounted on the Clay-Magellan 6.5 m telescope at Las Campanas Observatory. The observations were obtained on 2016 June 22 and 27 in clear weather and with median seeing ranging between about 0.″9 and 1.″2. All observations utilized the same instrument configuration, which included binning both CCDs 1 × 2 (dispersion × spatial) with four amplifiers in a slow readout mode. The "red" and "blue" spectrographs were each configured in high-resolution mode, and the 1.″2 fibers, 125 μm slits, and echelle gratings produced a typical resolving power of $R \equiv \lambda/\Delta\lambda \approx 27{,}000$. We also employed the "Bulge_GC1" order blocking filters that provide six consecutive orders spanning $\sim$6120–6720 Å at the cost of only using 48 of the possible 256 fibers.

Potential target stars were identified using J and K_S photometry available from the Two Micron All Sky Survey (2MASS; Skrutskie et al. 2006). We selected stars with J–K_S colors of 0.7–1.1 mag and K_S ranging from 10.0 to 11.8 mag. These selection criteria are equivalent to a range of about 1.1–1.9 mag in B–V color and 13.5–15.7 mag in the V band, which we illustrate in Figure 1 using optical photometry from Alves et al. (2001). A broad color range was adopted in order to probe the possible existence of intrinsic metallicity variations in the cluster. However, Figure 1 shows that all of the stars redder than the formal RGB were determined to have radial velocities inconsistent with cluster membership (see Section 3). We note also that two stars with high membership probabilities (2MASS 15460024–3748232 and 2MASS 15460078–3745426) may be bluer and brighter than the formal RGB and AGB sequences, and as a consequence they could be post-AGB stars.

The coordinates for all targets were obtained from the 2MASS catalog, and we were able to place fibers on 43 stars and five sky positions using a single configuration. Fibers were assigned to targets ranging from about 0.′8 to 8′ from the cluster center, but the member stars were only found inside $\sim$3.′5. Stars inside $\sim$0.′8 were avoided in order to mitigate the effects of blending and scattered light. With respect to the Alves et al. (2001) observations, we observed approximately 18% of all possible cluster stars with B–V in the range of 1.1–1.9 mag and with V between 13.5 and 16.0 mag. The star names, coordinates, and photometry for all target stars are provided in Table 1. The evolutionary state, based on a visual inspection of Figure 1, is also provided in Table 1 for the member stars.

2.1. Data Reduction

The data reduction procedure followed the methods outlined by Johnson et al. (2015a), in which the IRAF[10] tasks *CCDPROC*, *zerocombine*, and *darkcombine* were used to trim the overscan regions, create master bias and dark frames, and

[8] [A/B] $\equiv \log(N_A/N_B)_{star} - \log(N_A/N_B)_{\odot}$ and $\log\ \epsilon(A) \equiv \log(N_A/N_H) + 12.0$ for elements A and B.

[9] Note that the metallicity spreads for some clusters are disputed (Mucciarelli et al. 2015b, 2015c; Lardo et al. 2016; but see also Lee 2016).

[10] IRAF is distributed by the National Optical Astronomy Observatory, which is operated by the Association of Universities for Research in Astronomy, Inc., under cooperative agreement with the National Science Foundation.

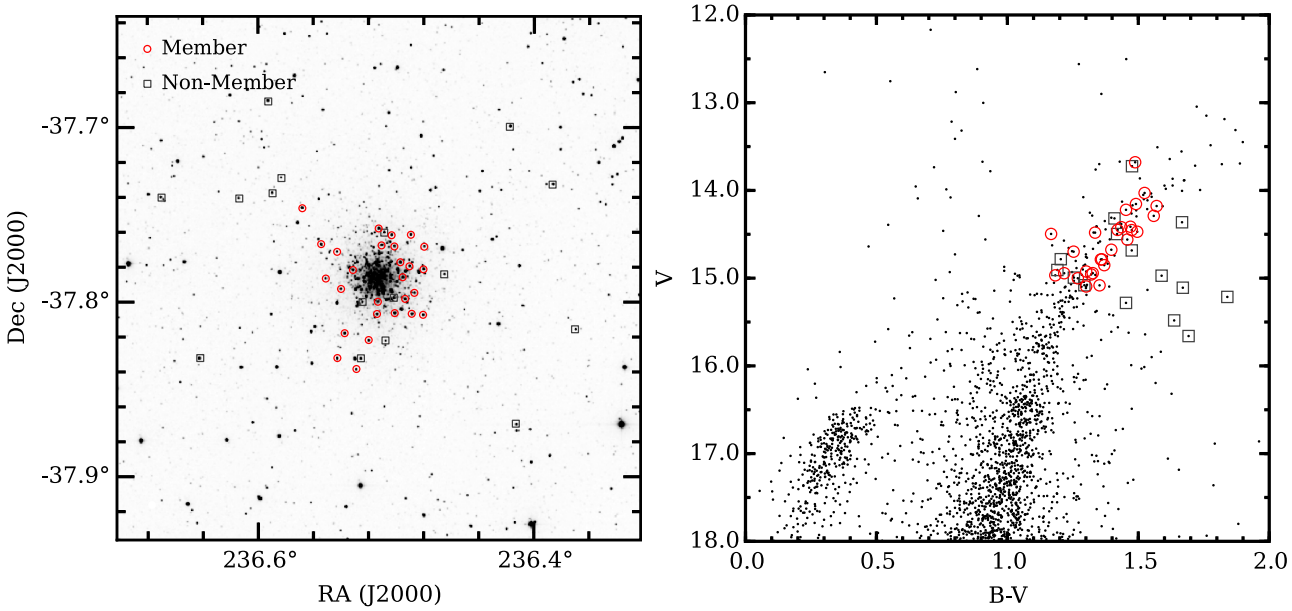

Figure 1. Left: 2MASS (Skrutskie et al. 2006) *J*-band image of NGC 5986. The radial velocity members and nonmembers identified in this work are indicated by open red circles and open gray boxes, respectively. Right: *V* vs. *B*–*V* color–magnitude diagram from Alves et al. (2001) shown with the same member and nonmember stars identified.

remove the bias and dark current effects. These basic data reduction tasks were performed independently on each amplifier frame. The reduced images were then rotated and transposed using the *imtranspose* task and combined via the *imjoin* routine to create one full monolithic image per CCD per exposure.

The remaining tasks of aperture tracing, flat-field correcting, scattered-light removal, wavelength calibration, cosmic-ray cleaning, and spectrum extraction were carried out using the *dohydra* task. Master sky spectra for each exposure set were created by scaling and combining the extracted sky fiber spectra, which were then subtracted from the object exposures. The final sky-subtracted images were continuum normalized and combined after removing the heliocentric velocities from each exposure and dividing by a high signal-to-noise ratio (S/N) telluric spectrum. The final combined spectra had typical S/Ns of approximately 100–200 per resolution element.

3. Radial Velocities and Cluster Membership

The radial velocities for all stars were calculated using the XCSAO (Kurtz & Mink 1998) cross-correlation routine. The synthetic spectrum of a cool metal-poor giant, smoothed and resampled to match the observations, was used as the reference template, and a heliocentric radial velocity value was independently determined for every order of each exposure. However, we avoided regions with very strong lines (e.g., Hα) and those where residual telluric features may still be present (e.g., 6270–6320 Å). The heliocentric radial velocity values listed in Table 1 represent the average velocity measurements of each order and exposure per star. Similarly, the velocity error values in Table 1 represent the standard deviation of all radial velocity measurements for each star. The average measurement uncertainties in Table 1 are 0.27 km s^{-1} (σ = 0.07 km s^{-1}) for the cluster members and 0.51 km s^{-1} (σ = 0.27 km s^{-1}) for the nonmembers.

Despite being a relatively massive cluster, very little kinematic information is available for NGC 5986. Previous work estimated the systemic heliocentric radial velocity of NGC 5986 to be $\sim$+90–97 km s^{-1} with a dispersion of $\sim$6–8 km s^{-1} (Hesser et al. 1986; Rutledge et al. 1997; Jasniewicz et al. 2004; Moni Bidin et al. 2009). In general, we find agreement with past work, but we measure a higher heliocentric radial velocity of +99.76 km s^{-1} for NGC 5986 and a velocity dispersion of 7.44 km s^{-1}. For the nonmember stars, we measure an average heliocentric radial velocity of −0.48 km s^{-1} (σ = 60.24 km s^{-1}).

As can be seen in Figure 2, the cluster and field star populations have clearly distinct velocity distributions. However, we note that the star 2MASS 15455164–3747031 is likely a foreground interloper. This star has a velocity of +105.81 km s^{-1}, which is nominally consistent with cluster membership but is significantly redder than the fiducial RGB sequence shown in Figure 1. Therefore, we have classified 2MASS 15455164–3747031 as a nonmember in Table 1 and do not consider it further. Using the final membership assignments outlined in Table 1, we find 63% (27/43 stars) of the stars in our sample to be likely cluster members.

4. Analysis

4.1. Stellar Parameters and Abundance Determinations

The analysis procedure adopted here closely follows the methods outlined in Johnson et al. (2015b) and includes use of the same line lists, reference solar abundance ratios, equivalent width (EW) measuring software, grid of α-enhanced ATLAS9 model atmospheres (Castelli & Kurucz 2004),[11] and local thermodynamic equilibrium (LTE) line analysis code MOOG[12] (Sneden 1973; 2014 version). On average, we measured approximately 40 Fe I and 5 Fe II lines per star, and we used the EW values of both species and the *abfind* driver in MOOG

[11] The model atmosphere grid can be downloaded from http://wwwuser.oats.inaf.it/castelli/grids.html.

[12] The MOOG source code is available at http://www.as.utexas.edu/~chris/moog.html.

Table 1
Star Identifiers, Coordinates, Photometry, and Velocities

Star Name (2MASS)	Alt. ID[a]	R.A. (deg)	Decl. (deg)	B (mag)	V (mag)	J (mag)	H (mag)	K_S (mag)	$RV_{helio.}$ (km s^{-1})	$RV_{helio.}$ Error (km s^{-1})	Evol. State
Cluster Members											
15455510−3746063	153	236.479603	−37.768421	16.396	15.095	12.406	11.750	11.597	104.99	0.42	RGB
15455524−3746528	55	236.480173	−37.781353	15.646	14.155	11.277	10.568	10.371	107.77	0.21	AGB
15455531−3748266	85	236.480472	−37.807415	15.816	14.481	11.812	11.145	11.008	95.30	0.33	AGB
15455682−3747414	83	236.486777	−37.794834	15.967	14.471	11.555	10.837	10.655	100.24	0.24	RGB
15455728−3748245	90	236.488681	−37.806828	16.018	14.560	11.686	10.940	10.776	111.04	0.28	RGB
15455743−3745416	80	236.489299	−37.761562	15.871	14.450	11.635	10.909	10.698	102.67	0.21	RGB
15455768−3746466	111	236.490334	−37.779633	16.147	14.786	12.035	11.347	11.196	93.90	0.23	RGB
15455843−3747538	81	236.493468	−37.798294	15.927	14.452	11.575	10.844	10.655	92.88	0.19	RGB
15455886−3747091	127	236.495254	−37.785885	16.161	14.944	12.367	11.742	11.534	102.25	0.35	AGB
15455926−3746383	77	236.496932	−37.777321	15.884	14.414	11.475	10.780	10.584	90.17	0.24	RGB
15460024−3748232	25	236.501022	−37.806450	15.167	13.679	10.888	10.214	10.022	101.60	0.22	Post−AGB?
15460030−3746057	78	236.501274	−37.768265	15.854	14.419	11.562	10.884	10.679	83.96	0.24	RGB
15460078−3745426	86	236.503273	−37.761837	15.663	14.496	11.714	11.055	10.869	103.40	0.24	Post−AGB?
15460253−3746035	132	236.510547	−37.767647	16.151	14.968	12.477	11.886	11.737	84.93	0.33	AGB
15460303−3745286	45	236.512634	−37.757965	15.553	14.029	11.112	10.418	10.231	110.23	0.19	AGB
15460317−3747598	126	236.513216	−37.799950	16.269	14.943	12.326	11.676	11.501	93.68	0.33	RGB
15460332−3748249	99	236.513847	−37.806942	16.073	14.676	11.921	11.184	11.040	96.90	0.21	RGB
15460476−3749186	112	236.519865	−37.821861	16.144	14.787	12.038	11.365	11.188	101.56	0.24	RGB
15460690−3750184	152	236.528773	−37.838455	16.434	15.082	12.480	11.700	11.538	98.94	0.36	RGB
15460751−3746542	60	236.531298	−37.781746	15.674	14.221	11.387	10.683	10.458	113.51	0.24	AGB
15460895−3749046	57	236.537307	−37.817947	15.748	14.178	11.174	10.418	10.247	101.88	0.26	RGB
15460957−3747333	102	236.539912	−37.792603	15.951	14.698	12.108	11.477	11.366	97.21	0.43	AGB
15461022−3749558	116	236.542585	−37.832172	16.222	14.852	12.066	11.381	11.221	94.54	0.28	RGB
15461025−3746168	123	236.542741	−37.771343	16.225	14.924	12.318	11.635	11.506	107.23	0.25	RGB
15461222−3747118	140	236.550938	−37.786636	16.270	15.001	12.396	11.717	11.562	108.25	0.34	RGB
15461303−3746009	129	236.554316	−37.766926	16.278	14.958	12.264	11.627	11.448	97.89	0.25	RGB
15461630−3744468	65	236.567931	−37.746349	15.849	14.290	11.238	10.460	10.337	96.71	0.21	RGB
Nonmembers											
15452886−3748562	270	236.370278	−37.815613	17.352	15.660	12.433	11.811	11.598	28.98	1.25	…
15453279−3743579	176	236.386664	−37.732777	17.054	15.214	11.784	10.945	10.717	−1.95	0.39	…
15453914−3752110	135	236.413115	−37.869740	16.561	14.972	12.285	11.683	11.548	8.96	0.58	…
15454023−3741589	87	236.417660	−37.699699	15.916	14.497	11.822	11.114	10.978	−10.28	0.39	…
15455164−3747031	158	236.465173	−37.784206	16.779	15.109	12.301	11.696	11.491	105.81	1.06	…
15460039−3747517	110	236.501659	−37.797695	15.988	14.784	12.330	11.742	11.568	−46.47	0.24	…
15460184−3749195	151	236.507702	−37.822098	16.375	15.081	12.397	11.756	11.558	−38.94	0.44	…
15460206−3745372	69	236.508607	−37.760357	15.728	14.319	11.579	10.853	10.713	146.82	0.43	…
15460582−3748002	121	236.524272	−37.800072	16.098	14.907	12.389	11.792	11.647	46.02	0.54	…
15460612−3749563	100	236.525510	−37.832314	16.159	14.684	11.714	11.058	10.861	−36.50	0.54	…
15461993−3743446	139	236.583058	−37.729076	16.248	14.994	12.452	11.824	11.721	−28.73	0.31	…
15462147−3744159	194	236.589484	−37.737766	16.735	15.282	12.403	11.641	11.509	8.47	0.29	…
15462221−3741066	71	236.592569	−37.685184	16.030	14.363	11.231	10.471	10.277	−2.99	0.49	…
15462726−3744267	228	236.613608	−37.740757	17.119	15.482	12.293	11.462	11.231	−36.84	0.47	…
15463408−3749556	30	236.642030	−37.832115	15.200	13.724	11.012	10.330	10.169	−77.36	0.40	…
15464077−3744246	…	236.669894	−37.740177	…	…	12.120	11.561	11.376	−72.71	0.38	…

Note.
[a] Identifiers are from Alves et al. (2001).

to iteratively solve for the model atmosphere parameters, such as effective temperature ($T_{\rm eff}$), surface gravity (log(g)), metallicity ([M/H]), and microturbulence ($\xi_{\rm mic.}$). In particular, the $T_{\rm eff}$ values were determined by removing trends in plots of log ϵ(Fe I) versus excitation potential, log(g) was estimated by enforcing ionization equilibrium between Fe I and Fe II, $\xi_{\rm mic.}$ was set by removing trends in plots of log ϵ(Fe I) versus log (EW/λ), and the model metallicity was set to the measured [Fe/H] abundance. A list of the adopted model atmosphere parameters for each star is provided in Table 2. Note that for 2MASS 15455531–3748266 and 2MASS 15460957–3747333 we were unable to converge to a stable model atmosphere solution, and we do not consider these stars further.

Similar to the case of Fe I and Fe II, the abundances of Si I, Ca I, Cr I, and Ni I were determined by an EW analysis using the MOOG *abfind* driver, the model atmosphere parameters listed in Table 2, and the line list provided in Johnson et al. (2015b, their Table 2). On average, the Si I, Ca I, Cr I, and Ni I abundances were based on the measurements of four, six, two, and five lines, respectively. All abundances have been measured relative to the metal-poor giant Arcturus, which is done to help offset effects due to departures from LTE and 1D

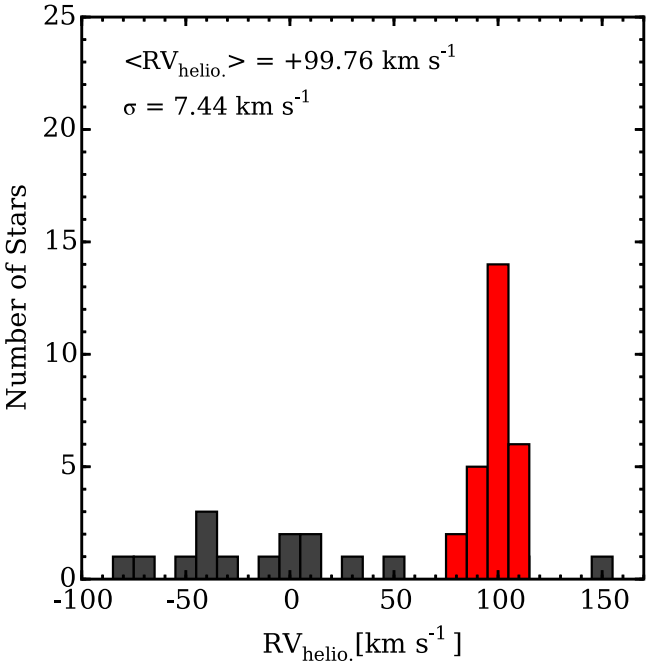

Figure 2. Heliocentric radial velocity distribution of all stars observed here, shown with bin sizes of 10 km s^{-1}. The radial velocity members are identified by the red bins, and the nonmembers are identified by the gray bins.

Table 2
Model Atmosphere Parameters

Star Name (2MASS)	$T_{\rm eff}$ (K)	log(g) (cgs)	[Fe/H] (dex)	$\xi_{\rm mic.}$ (km s^{-1})
15455510−3746063	4475	1.15	−1.59	1.70
15455524−3746528	4275	0.60	−1.60	1.90
15455531−3748266	…	…	…	…
15455682−3747414	4300	0.80	−1.57	1.80
15455728−3748245	4300	0.80	−1.49	1.65
15455743−3745416	4375	1.10	−1.46	1.80
15455768−3746466	4375	0.90	−1.65	1.80
15455843−3747538	4375	1.25	−1.52	1.95
15455886−3747091	4600	1.25	−1.58	1.65
15455926−3746383	4350	1.15	−1.42	1.75
15460024−3748232	4300	0.45	−1.66	1.80
15460030−3746057	4325	1.00	−1.52	1.80
15460078−3745426	4325	0.90	−1.57	1.50
15460253−3746035	4500	0.95	−1.71	1.55
15460303−3745286	4250	0.50	−1.62	1.95
15460317−3747598	4600	1.45	−1.46	1.60
15460332−3748249	4350	1.05	−1.63	1.85
15460476−3749186	4450	1.25	−1.50	1.65
15460690−3750184	4400	0.95	−1.61	1.65
15460751−3746542	4325	1.05	−1.52	1.85
15460895−3749046	4225	0.65	−1.53	1.95
15460957−3747333	…	…	…	…
15461022−3749558	4550	1.50	−1.45	1.85
15461025−3746168	4550	1.50	−1.45	1.60
15461222−3747118	4550	1.60	−1.49	1.70
15461303−3746009	4550	1.50	−1.49	1.80
15461630−3744468	4250	0.80	−1.53	2.00

versus 3D model atmosphere deficiencies. The final [Si/Fe], [Ca/Fe], [Cr/Fe], and [Ni/Fe] abundances for all member stars are provided in Tables 3–4.

For O I, Na I, Mg I, Al I, La II, and Eu II, the abundances have been determined via the *synth* spectrum synthesis module in MOOG. Similar to the EW analysis, the atomic and molecular line lists within 10 Å of each feature have been tuned to reproduce the Arcturus spectrum. Specifically, the log gf values and reference solar and Arcturus abundances for all species, except O I, are the same as those in Johnson et al. (2015b). Isotopic shifts and/or hyperfine broadening were accounted for with La II and Eu II using the line lists from Lawler et al. (2001a, 2001b). For oxygen, we used the [O I] λ6300.3 line and adopted the same atomic parameters and reference abundances as those provided by Johnson et al. (2014, their Table 2). Although Dupree et al. (2016) showed that the λ6300.3 feature can be affected by a star's chromosphere, the present data set does not provide enough information to reliably constrain a chromospheric model. Therefore, the oxygen abundances presented here are based only on radiative/convective equilibrium models.

All elements measured via spectrum synthesis included the updated CN line lists from Sneden et al. (2014), and the local CN lines were fit by fixing [C/Fe] = −0.3, holding [O/Fe] at the best-fit value determined from the λ6300.3 line, and treating the N abundance as a free parameter. The Mg I λ6319 triplet required additional care because the lines are relatively weak and can be affected by a broad Ca I autoionization feature. We modeled the impact of the autoionization line by artificially modifying the log ϵ(Ca) abundance during each synthesis such that the slope of the continuum around the Mg I lines was well fit. The final [O/Fe], [Na/Fe], [Mg/Fe], [Al/Fe], [La/Fe], and [Eu/Fe] abundances for all member stars are provided in Tables 3–4, but are based on an average of only one to two lines for each element.

4.2. Model Atmosphere Parameter and Abundance Uncertainties

We investigated uncertainties in the model atmosphere parameters using comparisons between spectroscopic and photometric $T_{\rm eff}$ and log(g) values, by investigating the typical residual scatter present in plots of log ϵ(Fe I) versus log(EW/λ), and by examining the typical line-to-line scatter in the derived log ϵ(Fe I) and log ϵ(Fe II) abundances. In order to estimate stellar parameters from photometry, we have to assume a cluster distance and reddening. Ortolani et al. (2000) and Alves et al. (2001) estimate distances of 11.2 and 10.7 kpc, respectively, and for this work we have adopted a distance of 10.7 kpc. For the reddening, we note that while the differential reddening toward NGC 5986 is relatively low (Alves et al. 2001), the absolute reddening value is moderately high, with literature estimates ranging from approximately $E(B–V) = 0.22$ to 0.36 mag (Zinn 1980; Bica & Pastoriza 1983; Rosenberg et al. 2000; Alves et al. 2001; Recio-Blanco et al. 2005). We initially assumed $E(B–V) = 0.29$ mag, which is the mean of the full literature range, but subsequent tests showed that the best agreement between the spectroscopic and photometric $T_{\rm eff}$ values occurred with $E(B–V) = 0.33$ mag.

Using the V magnitudes from Alves et al. (2001) and the 2MASS J and K_S magnitudes, we followed the photometric transformation procedure outlined in Johnson et al. (2005; see their Section 3.1) to obtain photometric temperatures for all NGC 5986 members. Assuming $E(B–V) = 0.33$ mag, we found the star-to-star dispersion to be 72 K. Similarly, assuming a distance of 10.7 kpc and a typical stellar mass of 0.8 $M_\odot$,[13] we

[13] Although we are assuming the same mass for all stars in the photometric surface gravity calculation, Figure 1 shows that several stars are likely on the AGB and may have masses of ∼0.6 $M_\odot$. However, the photometric gravity is only sensitive to log($M/M_\odot$) so the difference in log(g) is only ∼0.10 dex.

Table 3
Chemical Abundances and Uncertainties: O–Ca

Star Name (2MASS)	[O I/Fe] (dex)	Δ[O I/Fe] (dex)	[Na I/Fe] (dex)	Δ[Na I/Fe] (dex)	[Mg I/Fe] (dex)	Δ[Mg I/Fe] (dex)	[Al I/Fe] (dex)	Δ[Al I/Fe] (dex)	[Si I/Fe] (dex)	Δ[Si I/Fe] (dex)	[Ca I/Fe] (dex)	Δ[Ca I/Fe] (dex)
15455510−3746063	0.62	0.10	0.20	0.09	0.31	0.05	0.39	0.07	0.42	0.13	0.31	0.07
15455524−3746528	0.45	0.10	0.04	0.12	0.22	0.04	0.47	0.11	0.21	0.11	0.26	0.07
15455531−3748266	…	…	…	…	…	…	…	…	…	…	…	…
15455682−3747414	−0.25	0.10	0.47	0.06	−0.01	0.07	1.24	0.06	0.49	0.11	0.32	0.05
15455728−3748245	0.27	0.10	0.23	0.04	0.31	0.07	0.52	0.13	0.17	0.15	0.24	0.06
15455743−3745416	0.34	0.10	0.22	0.14	0.18	0.06	0.88	0.07	0.32	0.11	0.31	0.06
15455768−3746466	0.60	0.10	−0.10	0.08	0.50	0.03	0.07	0.06	0.33	0.12	0.33	0.06
15455843−3747538	0.69	0.10	0.17	0.03	0.44	0.05	0.12	0.07	0.31	0.11	0.28	0.05
15455886−3747091	0.51	0.10	0.16	0.06	0.15	0.05	0.37	0.07	0.39	0.12	0.24	0.06
15455926−3746383	0.63	0.10	0.11	0.08	0.34	0.05	0.35	0.07	0.30	0.12	0.30	0.05
15460024−3748232	0.37	0.10	0.27	0.04	0.44	0.05	0.32	0.07	0.29	0.11	0.28	0.07
15460030−3746057	0.49	0.10	0.19	0.03	0.35	0.05	0.51	0.07	0.35	0.18	0.25	0.05
15460078−3745426	0.68	0.10	−0.13	0.19	0.40	0.03	0.16	0.07	0.37	0.11	0.26	0.06
15460253−3746035	0.32	0.10	0.30	0.08	0.24	0.05	0.43	0.10	0.43	0.12	0.15	0.06
15460303−3745286	0.62	0.10	−0.18	0.06	0.33	0.04	−0.25	0.05	0.25	0.11	0.29	0.06
15460317−3747598	0.44	0.10	0.39	0.11	0.33	0.05	0.90	0.05	0.44	0.11	0.22	0.06
15460332−3748249	0.58	0.10	0.11	0.07	0.40	0.03	0.19	0.07	0.37	0.11	0.30	0.06
15460476−3749186	0.72	0.10	−0.27	0.09	0.32	0.05	0.10	0.07	0.26	0.12	0.19	0.06
15460690−3750184	0.31	0.10	0.28	0.03	0.28	0.05	0.62	0.05	0.40	0.11	0.29	0.06
15460751−3746542	0.31	0.10	0.34	0.08	0.18	0.05	0.65	0.07	0.32	0.12	0.27	0.06
15460895−3749046	0.49	0.10	−0.28	0.08	0.40	0.05	0.21	0.07	0.46	0.12	0.33	0.06
15460957−3747333	…	…	…	…	…	…	…	…	…	…	…	…
15461022−3749558	…	…	0.17	0.03	0.30	0.05	0.57	0.07	0.27	0.11	0.21	0.05
15461025−3746168	…	…	0.18	0.03	…	…	0.66	0.04	0.21	0.11	0.22	0.06
15461222−3747118	0.13	0.10	0.33	0.03	0.05	0.05	1.00	0.10	0.38	0.12	0.26	0.06
15461303−3746009	0.19	0.10	0.46	0.08	0.01	0.05	1.07	0.07	0.44	0.12	0.26	0.06
15461630−3744468	0.56	0.10	0.03	0.08	0.35	0.05	0.35	0.05	0.36	0.11	0.30	0.06

Table 4
Chemical Abundances and Uncertainties: Cr–Eu

Star Name (2MASS)	[Cr I/Fe] (dex)	Δ[Cr I/Fe] (dex)	[Fe I/H] (dex)	Δ[Fe I/H] (dex)	[Fe II/H] (dex)	Δ[Fe II/H] (dex)	[Ni I/Fe] (dex)	Δ[Ni I/Fe] (dex)	[La II/Fe] (dex)	Δ[La II/Fe] (dex)	[Eu II/Fe] (dex)	Δ[Eu II/Fe] (dex)
15455510−3746063	0.05	0.09	−1.59	0.10	−1.58	0.12	−0.14	0.07	0.52	0.10	0.68	0.10
15455524−3746528	−0.08	0.07	−1.60	0.10	−1.60	0.12	−0.12	0.06	0.34	0.10	0.62	0.10
15455531−3748266	…	…	…	…	…	…	…	…	…	…	…	…
15455682−3747414	0.07	0.05	−1.57	0.10	−1.57	0.13	−0.16	0.06	0.38	0.10	0.67	0.10
15455728−3748245	0.08	0.06	−1.49	0.10	−1.48	0.11	−0.14	0.06	0.24	0.10	0.76	0.11
15455743−3745416	0.06	0.06	−1.46	0.10	−1.46	0.13	−0.14	0.06	0.51	0.10	0.89	0.11
15455768−3746466	0.10	0.06	−1.65	0.10	−1.65	0.12	−0.02	0.06	0.23	0.10	0.70	0.15
15455843−3747538	−0.02	0.05	−1.52	0.10	−1.51	0.12	−0.06	0.05	0.53	0.10	0.95	0.12
15455886−3747091	…	…	−1.58	0.10	−1.58	0.11	−0.17	0.07	0.23	0.11	0.79	0.10
15455926−3746383	0.02	0.05	−1.42	0.10	−1.42	0.13	−0.07	0.07	0.46	0.10	0.79	0.10
15460024−3748232	…	…	−1.67	0.10	−1.64	0.12	−0.20	0.05	0.36	0.11	0.69	0.10
15460030−3746057	0.07	0.05	−1.51	0.10	−1.52	0.11	−0.18	0.05	0.53	0.10	0.79	0.10
15460078−3745426	−0.05	0.06	−1.58	0.10	−1.56	0.13	−0.14	0.05	0.35	0.15	0.69	0.10
15460253−3746035	0.14	0.06	−1.72	0.10	−1.69	0.12	−0.13	0.06	0.53	0.11	0.68	0.10
15460303−3745286	−0.03	0.06	−1.61	0.10	−1.62	0.12	−0.16	0.06	0.32	0.11	0.66	0.10
15460317−3747598	0.02	0.06	−1.46	0.10	−1.46	0.13	0.03	0.15	0.34	0.15	0.82	0.10
15460332−3748249	0.08	0.06	−1.63	0.10	−1.62	0.11	−0.17	0.07	0.49	0.10	0.74	0.10
15460476−3749186	0.06	0.06	−1.50	0.10	−1.50	0.12	−0.12	0.06	0.48	0.14	0.76	0.11
15460690−3750184	0.04	0.06	−1.61	0.10	−1.60	0.11	−0.15	0.10	0.29	0.11	0.71	0.10
15460751−3746542	0.02	0.06	−1.51	0.10	−1.52	0.12	−0.14	0.05	0.43	0.10	0.81	0.10
15460895−3749046	0.00	0.06	−1.53	0.10	−1.53	0.13	−0.10	0.07	0.35	0.10	0.75	0.10
15460957−3747333	…	…	…	…	…	…	…	…	…	…	…	…
15461022−3749558	0.11	0.05	−1.45	…	−1.45	0.11	−0.12	0.06	0.59	0.10	0.95	0.14
15461025−3746168	−0.07	0.06	−1.44	…	−1.45	0.13	−0.22	0.06	0.48	0.12	0.80	0.10
15461222−3747118	0.18	0.06	−1.48	0.10	−1.49	0.13	−0.13	0.07	0.49	0.11	0.80	0.18
15461303−3746009	0.05	0.06	−1.49	0.10	−1.49	0.12	−0.03	0.07	0.59	0.10	0.79	0.12
15461630−3744468	0.09	0.06	−1.53	0.10	−1.53	0.12	−0.11	0.05	0.42	0.10	0.77	0.10

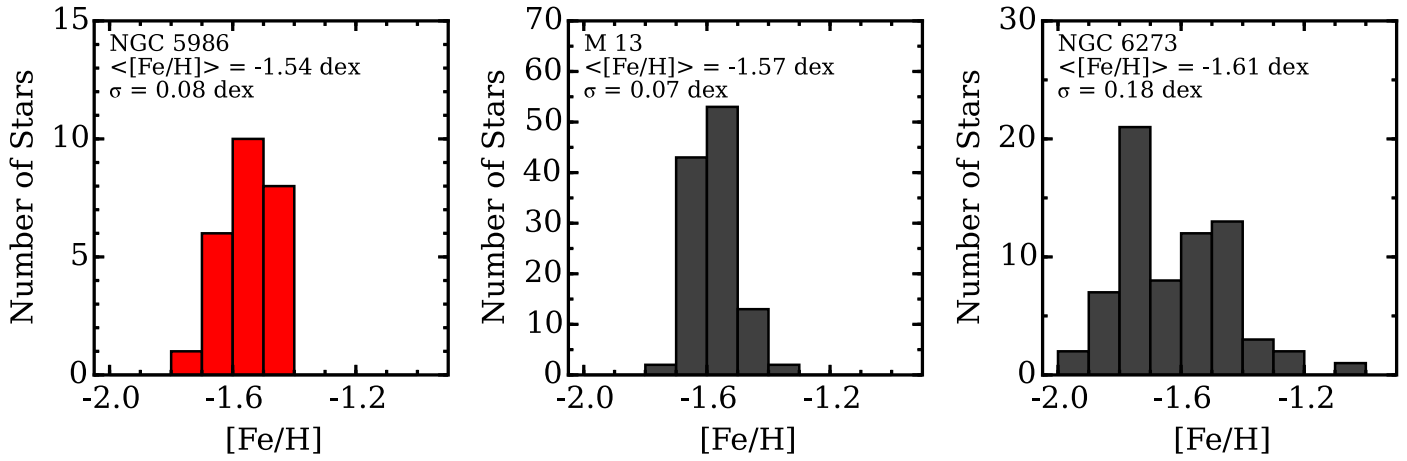

Figure 3. Comparison of the metallicity distribution functions of NGC 5986 (left panel), M13 (Johnson & Pilachowski 2012; middle panel), and NGC 6273 (Johnson et al. 2015b, 2017; right panel), which were derived using similar methods and line lists and also exhibit similar mean metallicities. The [Fe/H] abundance spread for NGC 5986 is consistent with other monometallic clusters, such as M13. The data for all three clusters are sampled into 0.10 dex bins.

found the average difference in photometric and spectroscopic gravities to be 0.08 dex in log(g), with a dispersion of 0.22 dex. Therefore, we have adopted $\Delta T_{\rm eff}$ and $\Delta\log(g)$ of 75 K and 0.20 dex, respectively, as typical uncertainty values. For the model metallicity uncertainties, we found the average line-to-line scatter in log ϵ(Fe I) and log ϵ(Fe II) to be 0.10 dex ($\sigma = 0.02$ dex) and 0.11 dex ($\sigma = 0.04$ dex), respectively. We have adopted 0.10 dex as the typical uncertainty in a star's model atmosphere metallicity. Finally, an examination of the line-to-line scatter in plots of log ϵ(X) versus log(EW/λ) suggests that the typical microturbulence uncertainty is approximately 0.10 km s^{-1}.

In order to estimate the impact of model atmosphere uncertainties on the abundance measurements, we redetermined the abundances of each element after changing $T_{\rm eff} \pm 75$ K, log (g) $\pm$ 0.20 dex, [Fe/H] $\pm$ 0.10 dex,[14] and $\xi_{\rm mic.} \pm 0.10$ km s^{-1}. Abundance uncertainty terms were calculated for each element by individually varying the model atmosphere parameters while holding the other values fixed. The abundance uncertainties due to varying each model atmosphere parameter were then added in quadrature, along with the line-to-line measurement uncertainties, and are provided in Tables 3–4.

Finally, we note that an investigation into trends of [X/Fe] versus $T_{\rm eff}$ and [Fe/H] revealed that minor trends may exist between [Ca/Fe] and $T_{\rm eff}$ and between [Eu/Fe] and [Fe/H]. For Ca, we find that stars with $T_{\rm eff} < 4400$ K have $\langle$[Ca/Fe]$\rangle = +0.29$ dex ($\sigma = 0.03$ dex) while those with $T_{\rm eff} > 4400$ K have $\langle$[Ca/Fe]$\rangle = +0.23$ dex ($\sigma = 0.03$ dex). However, the star-to-star dispersion in [Ca/Fe] is only 0.04 dex for the entire sample, and we did not find any trends between $T_{\rm eff}$ and log ϵ(Fe I), log ϵ(Fe II), or log ϵ(Ca I). Combined with the paucity of similar trends between $T_{\rm eff}$ and any other [X/Fe] ratios, we believe that the mild correlation between $T_{\rm eff}$ and [Ca/Fe] is insignificant.

The correlation between [Eu/Fe] and [Fe/H] is more troubling as stars with [Fe/H] < -1.55 have $\langle$[Eu/Fe]$\rangle = +0.69$ dex ($\sigma = 0.04$ dex) and those with [Fe/H] > -1.55 have $\langle$[Eu/Fe]$\rangle = +0.81$ dex ($\sigma = 0.07$ dex). Since the other elements examined here do not exhibit similarly strong correlations with [Fe/H], we do not have a clear explanation for the behavior of [Eu/Fe]. For example, a simple explanation such as improperly accounting for a blend of the Si I line at 6437.71 Å and the Eu II line at 6437.64 Å is unlikely because [Si/Fe] is not correlated with [Fe/H] or [Eu/Fe]. In any case, we caution the reader that the observed star-to-star variation of ~0.1 dex presented here for [Eu/Fe] may be an overestimate.

[14] Note that the use of α-enhanced model atmospheres largely compensates for differences between the iron abundance ([Fe/H]) and overall metallicity ([M/H]).

5. Results and Discussion

5.1. Metallicity Distribution Function

As mentioned in Section 1, the analysis of two AGB/post-AGB stars by Jasniewicz et al. (2004), which found a cluster metallicity of [Fe/H] ~ -1.65, represents the only detailed chemical composition measurement of individual stars in NGC 5986. However, previous and subsequent photometric analyses have found in agreement that the cluster has a mean metallicity of [Fe/H] ~ -1.60 (Bica & Pastoriza 1983; Geisler et al. 1997; Ortolani et al. 2000; Dotter et al. 2010). In this work, we measured [Fe/H] for 25 RGB and AGB stars and derived a similar mean metallicity of $\langle$[Fe/H]$\rangle = -1.54$ dex ($\sigma = 0.08$ dex).

Interestingly, although NGC 5986 has a mean metallicity, present-day mass, and horizontal branch morphology that are similar to those of several iron-complex clusters, its comparatively small [Fe/H] dispersion likely precludes the cluster from being a member of the iron-complex class. For example, Figure 3 compares the [Fe/H] distributions of the monometallic cluster M13, the iron-complex cluster NGC 6273, and NGC 5986. All three clusters exhibit extended blue horizontal branches, are relatively massive, and have comparable mean [Fe/H] values, but Figure 3 shows that NGC 5986 lacks the broad [Fe/H] spread that is a defining characteristic of iron-complex clusters. Instead, NGC 5986 appears to be a more typical monometallic cluster, similar to M13.

5.2. Basic Chemical Composition Results

A summary of the chemical abundances found in NGC 5986 is provided as a box plot in Figure 4. Similar to other old globular clusters (see, e.g., reviews by Kraft 1994; Gratton et al. 2004), the light elements O, Na, Mg, and Al exhibit the largest star-to-star abundance variations (see also Section 5.3). Additionally, the heavy

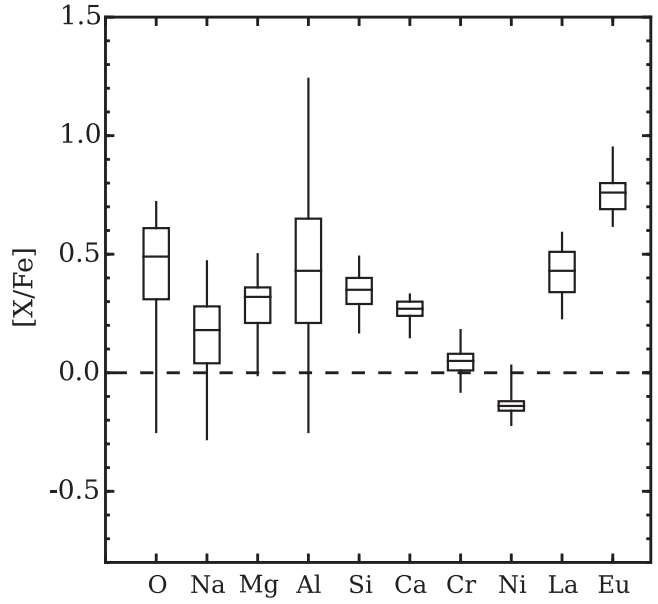

Figure 4. Box plot comparing the [X/Fe] distributions of all elements analyzed here for the NGC 5986 radial velocity member stars. For each element, the bottom, middle, and top horizontal lines indicate the first, second (median), and third quartile values, respectively. The extended vertical lines indicate the minimum and maximum [X/Fe] abundances. The black dashed line illustrates the solar abundance ratios.

α-elements are enhanced with $\langle$[Si/Fe]$\rangle = +0.34$ dex ($\sigma =$ 0.08 dex) and $\langle$[Ca/Fe]$\rangle = +0.27$ dex ($\sigma = 0.04$ dex), while the Fe-peak elements Cr and Ni have approximately solar ratios with $\langle$[Cr/Fe]$\rangle = +0.04$ dex ($\sigma = 0.06$ dex) and $\langle$[Ni/Fe]$\rangle =$ -0.12 dex ($\sigma = 0.06$ dex). Interestingly, the two neutron-capture elements La and Eu are both enhanced with $\langle$[La/Fe]$\rangle =$ $+0.42$ dex ($\sigma = 0.11$ dex) and $\langle$[Eu/Fe]$\rangle = +0.76$ dex ($\sigma =$ 0.08 dex). We detect a mild correlation between [La/Fe] and [Eu/Fe], and the full [X/Fe] range exhibited by each element is $\sim$0.35 dex. Following Roederer (2011), we consider NGC 5986 to be a borderline case that may possess a small intrinsic heavy-element dispersion.[15] However, the available data seem to rule out that NGC 5986 is similar to more extreme cases, such as M15, where the full range in [La/Fe] and [Eu/Fe] can span $>$0.6 dex (e.g., Sneden et al. 1997; Sobeck et al. 2011).

Although the present work represents the only large-sample chemical abundance analysis of cluster RGB stars, we note that Jasniewicz et al. (2004) measured O, Na, Mg, Si, Ca, Cr, Ni, La, and Eu abundances for two highly evolved AGB/post-AGB stars. In general, both studies agree that NGC 5986 stars have [α/Fe] $\sim +0.30$ dex, approximately solar [X/Fe] ratios for the Fe-peak elements, and enhanced [La/Fe] and [Eu/Fe] ratios. However, we find an average $\langle$[Na/Fe]$\rangle = +0.15$ dex, which is significantly lower than the [Na/Fe] $= +0.70$–1.00 dex ratios measured by Jasniewicz et al. (2004). The heavy neutron-capture element abundance pattern exhibited by the potential post-AGB star NGC 5986 ID7 in Jasniewicz et al. (2004) follows the same distribution as the RGB/AGB stars measured here. The low [La/Eu] ratios found in both studies suggest that NGC 5986 did not experience significant *s*-process enrichment, and therefore the enhanced [Zr/Fe], [La/Fe], [Ce/Fe], [Sm/Fe], and [Eu/Fe] abundances of ID7 may not necessarily reflect additional processing and/or mixing via third dredge-up.

In Figure 5, we compare the abundance pattern of NGC 5986 against several Milky Way globular clusters (see Table 5 for references) spanning a wide range in [Fe/H] and find that NGC 5986 has a composition that is nearly identical to other similar-metallicity clusters. In fact, only the cluster's [La/Fe] and [Eu/Fe] abundances deviate from the typical Galactic trend, with NGC 5986 stars exhibiting higher ratios; however, the cluster's heavy-element composition may bear some resemblance to that of M107 (O'Connell et al. 2011). The combination of enhanced [La/Fe] and [Eu/Fe] found in NGC 5986 also nearly matches the pattern found by Cavallo et al. (2004) for the similar-metallicity cluster M80, but a recent analysis by Carretta (2015) revised M80's mean [La/Fe] and [Eu/Fe] abundances downward by $\sim$0.3 dex.

To place NGC 5986 into context, Figure 6 extends the [Eu/Fe] panel of Figure 5 to include a comparison of the cluster against individual stars in the Galactic halo, thin/thick disk, bulge, and several Local Group classical and ultrafaint dwarf galaxies. Although it is not unusual to find strongly Eu-enhanced stars at [Fe/H] $\gtrsim -2$ dex, such objects are almost exclusively found in dwarf galaxies exhibiting large [Eu/Fe] dispersions. In contrast, NGC 5986 exhibits a mean [Eu/Fe] abundance that is comparable to some of the most Eu-enhanced stars in galaxies such as Fornax, Carina, Ursa Minor, and Draco, but the cluster's [Eu/Fe] dispersion is at least 1.5–2 times smaller. The data suggest that NGC 5986 was enriched by a high-yield *r*-process event (or events) and that the enriched gas was able to be rapidly mixed within the cluster.

Interestingly, the high [La/Fe] abundances of stars in NGC 5986 are similar to those found in the more metal-rich populations of the iron-complex clusters ω Cen (e.g., Norris & Da Costa 1995; Smith et al. 2000; Johnson & Pilachowski 2010; Marino et al. 2011a), NGC 5286 (Marino et al. 2015), M22 (Marino et al. 2009, 2011b), M2 (Yong et al. 2014b), NGC 1851 (Carretta et al. 2011), and NGC 6273 (Johnson et al. 2015b, 2017). The mean metallicity of NGC 5986 is comparable to the typical [Fe/H] values exhibited by the Fe/*s*-process-enhanced populations in several iron-complex clusters as well. For example, Figure 7 compares the spectrum of a star in NGC 5986 with the spectrum of an Fe/*s*-process-enhanced star in NGC 6273 of similar temperature, metallicity, and gravity and shows that both objects have comparable [Fe/H] and [La/Fe] abundances. However, Figure 7 also shows that the Eu II λ6645 line in the NGC 5986 star is considerably stronger than in the NGC 6273 star. The cluster's high [Eu/Fe] abundances and mean $\langle$[La/Eu]$\rangle = -0.34$ dex ($\sigma = 0.10$ dex) therefore follow the same *r*-process-dominated pattern exhibited by most monometallic clusters, precluding NGC 5986 from being an iron-complex cluster.

Figure 5 also compares the α-, Fe-peak-, and neutron-capture-element abundances of NGC 5986 and NGC 4833. Although NGC 4833 is significantly more metal-poor than NGC 5986 at [Fe/H] ≈ -2.15 (Carretta et al. 2014; Roederer & Thompson 2015), Casetti-Dinescu et al. (2007) found the two clusters to exhibit similar orbital properties and suggested that the clusters may share a common origin. With the present data, it is difficult to assess whether NGC 5986 and NGC 4833 are both chemically and dynamically linked. For example, Figure 5 shows that the two clusters share similar mean [Ca/Fe], [Ni/Fe], and [La/Eu] abundances, and we can also

[15] As discussed in Section 4.2, we detected a possible correlation between [Fe/H] and [Eu/Fe] that may be spurious and caution the reader that the cluster's true [Eu/Fe] dispersion may be smaller than the 0.08 dex value cited here.

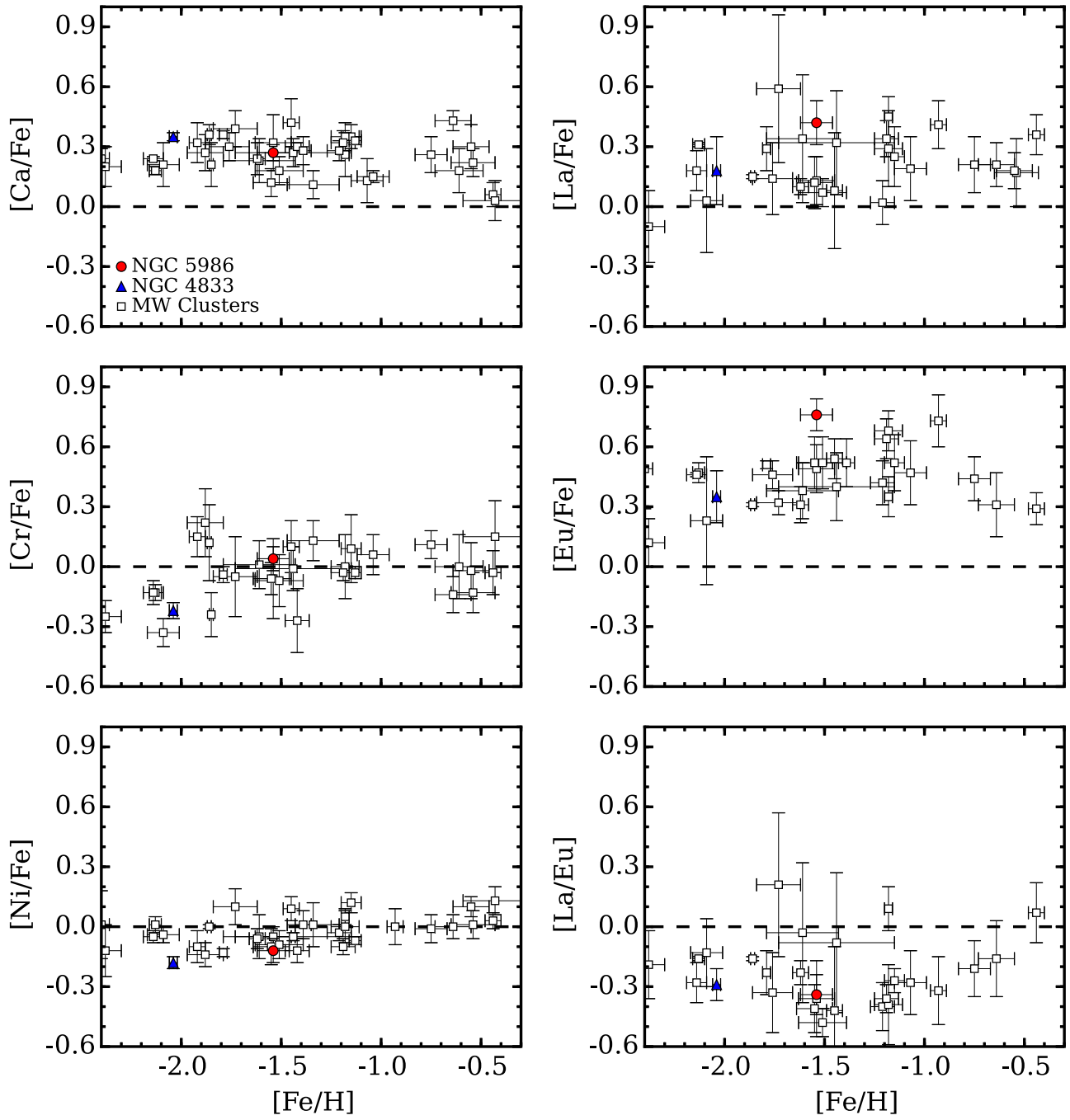

Figure 5. Average [Ca/Fe], [Cr/Fe], [Ni/Fe], [La/Fe], [Eu/Fe], and [La/Eu] abundances of NGC 5986 (filled red circles) and NGC 4833 (filled blue triangles) compared to those of several Galactic globular clusters (open squares) of different [Fe/H]. In all panels, the symbols indicate the cluster average values and the error bars show the star-to-star dispersions. The literature sources for each globular cluster are provided in Table 5.

note that both clusters may exhibit larger-than-average [Ca/Mg] dispersions (see also Section 5.3 here and Figure 15 of Carretta et al. 2014). In contrast, the clusters appear to have very different mean [Cr/Fe], [La/Fe], and [Eu/Fe] abundances. Therefore, NGC 5986 and NGC 4833 may exhibit larger cluster-to-cluster heavy-element abundance variations than are observed among similar-metallicity globular clusters associated with the Sagittarius system (e.g., Mottini et al. 2008; Sbordone et al. 2015). However, if NGC 5986 and NGC 4833 do originate from a common system, such as a dwarf galaxy, then the progenitor object may have followed a chemical enrichment path that differs from Sagittarius.

5.3. Light-element Abundance Variations

As mentioned in Section 5.2, the light elements O, Na, Mg, and Al exhibit significant star-to-star abundance variations, with Δ[X/Fe] ranging from 0.51 dex for [Mg/Fe] to 1.49 dex for [Al/Fe]. Additionally, Figure 8 shows that NGC 5986 exhibits a clear O–Na anticorrelation along with a strong Na–Al correlation. The O–Na and Na–Al relations are common features found in nearly all clusters with [Fe/H] $\lesssim -1$, and the presence of these (anti)correlations in stars at all evolutionary states (see Section 1) indicates that pollution, rather than in situ mixing, is the dominant mechanism driving the light-element

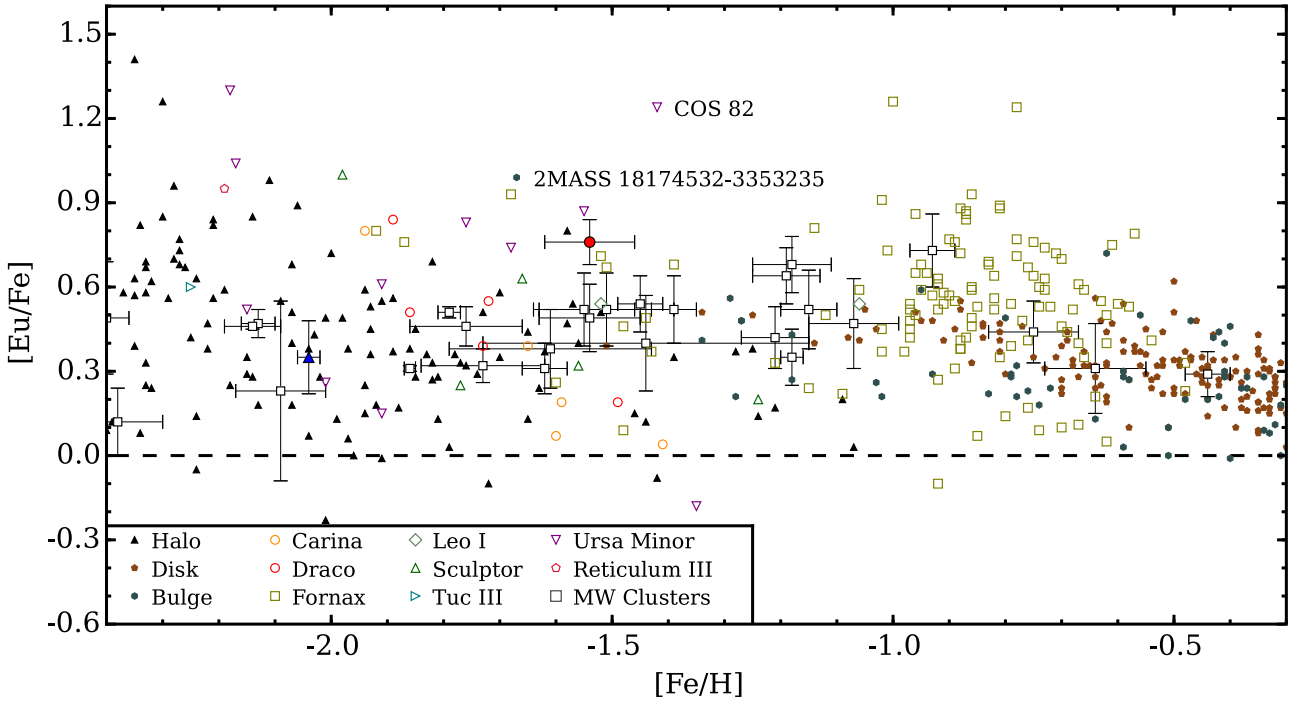

Figure 6. Mean [Eu/Fe] abundances of NGC 5986 (filled red circle), NGC 4833 (filled blue triangle), and several Galactic globular clusters (open squares with error bars) plotted as a function of [Fe/H]. The globular clusters are compared against similar composition measurements in the Galactic halo, disk, and bulge along with several classical and ultrafaint Local Group dwarf galaxies. The literature data for the halo, thin/thick disk, and bulge are compiled from Barklem et al. (2005), McWilliam et al. (2010), Johnson et al. (2012, 2013), Roederer et al. (2014), Battistini & Bensby (2016), and Van der Swaelmen et al. (2016). The dwarf galaxy data are from Shetrone et al. (2003) for Carina; Shetrone et al. (2001) and Cohen & Huang (2009) for Draco; Shetrone et al. (2003), Letarte et al. (2010), and Lemasle et al. (2014) for Fornax; Shetrone et al. (2003) for Leo I and Sculptor; Hansen et al. (2017) for Tucana III; Shetrone et al. (2001), Aoki et al. (2007), and Cohen & Huang (2010) for Ursa Minor; and Ji et al. (2016) for Reticulum II. The globular cluster data are the same as in Figure 5. Stars in the Galactic bulge and Ursa Minor dwarf galaxy that have [Fe/H] similar to NGC 5986 but [Eu/Fe] $\gtrsim +1$ are also identified in the plot.

abundance variations. In this sense, the simultaneous signature of O depletions with enhancements in Na and Al indicates that the gas from which the second-generation (O/Mg-poor, Na/Al-rich) stars formed was processed at temperatures of at least ∼45 MK (e.g., Prantzos et al. 2007, their Figure 2). However, a variety of pollution sources, such as intermediate-mass AGB stars (e.g., Ventura & D'Antona 2009; Doherty et al. 2014), rapidly rotating massive main-sequence stars (e.g., Decressin et al. 2007), massive interacting binary stars (de Mink et al. 2009), and supermassive stars (Denissenkov & Hartwick 2014), are capable of reaching these temperatures. Therefore, an examination of the interplay between Mg, Al, and Si, which are more sensitive to higher burning temperatures, can help shed light on which pollution mechanism(s) may have been active in NGC 5986 and other clusters.

The bottom panels of Figure 8 show that NGC 5986 exhibits a clear Mg–Al anticorrelation and Al–Si correlation. Unlike the more ubiquitous O–Na and Na–Al relations, the Mg–Al and Al–Si (anti)correlations are not found in all clusters. Instead, these chemical properties seem to be common only among massive and/or metal-poor clusters with extended blue horizontal branches, such as NGC 2808 (Carretta 2014, 2015), NGC 6752 (Yong et al. 2005; Carretta et al. 2012a), M15 (Sneden et al. 1997; Carretta et al. 2009a), M13 (Sneden et al. 2004; Cohen & Meléndez 2005), NGC 6273 (Johnson et al. 2015b, 2017), ω Cen (Norris & Da Costa 1995; Smith et al. 2000; Da Costa et al. 2013), M54 (Carretta et al. 2010c), NGC 1851 (Carretta et al. 2012b), NGC 4833 (Carretta et al. 2014; Roederer & Thompson 2015), M92 (Mészáros et al. 2015; Ventura et al. 2016), and NGC 6093 (Carretta et al. 2015). In NGC 5986 and similar clusters, the significant depletion of ^{24}Mg requires temperatures $\gtrsim$65–70 MK (e.g., Langer et al. 1997; Arnould et al. 1999; Prantzos et al. 2007). At these temperatures the ^{27}Al (p, γ)^{28}Si reaction rate exceeds that of the ^{27}Al(p, α)^{24}Mg reaction (see, e.g., Arnould et al. 1999, their Figure 8), and leakage from the Mg–Al cycle can produce small increases (∼0.1 dex) in [Si/Fe]. Therefore, despite significant uncertainties in several reaction rates (e.g., Izzard et al. 2007), the combined abundance patterns of O, Na, Mg, Al, and Si support the idea that the gas from which the second-generation stars in NGC 5986 formed likely experienced temperatures $\gtrsim$65–70 MK. Following D'Antona et al. (2016), we can conclude that only the AGB and/or supermassive star pollution scenarios mentioned above likely remain viable to explain the light-element patterns of NGC 5986; however, these scenarios still face substantial challenges in explaining all of the observed abundance patterns (e.g., Renzini et al. 2015).

In clusters such as NGC 2419 (Cohen & Kirby 2012; Mucciarelli et al. 2012) and NGC 2808 (Carretta 2015; Mucciarelli et al. 2015a), the O, Na, Mg, Al, and Si abundance (anti)correlations are accompanied by similar relations involving elements as heavy as K, Ca, and Sc. For these cases, Ventura et al. (2012) noted that the abundance patterns may be explained if proton-capture reactions operated in an environment where the burning temperatures exceeded ∼100 MK. Although we did not measure K and Sc abundances for NGC 5986, we note that Carretta et al. (2013b) and Carretta (2015) have shown that the [Ca/Mg] spread may be a reliable indicator for finding clusters that experienced extreme high-temperature processing. For NGC

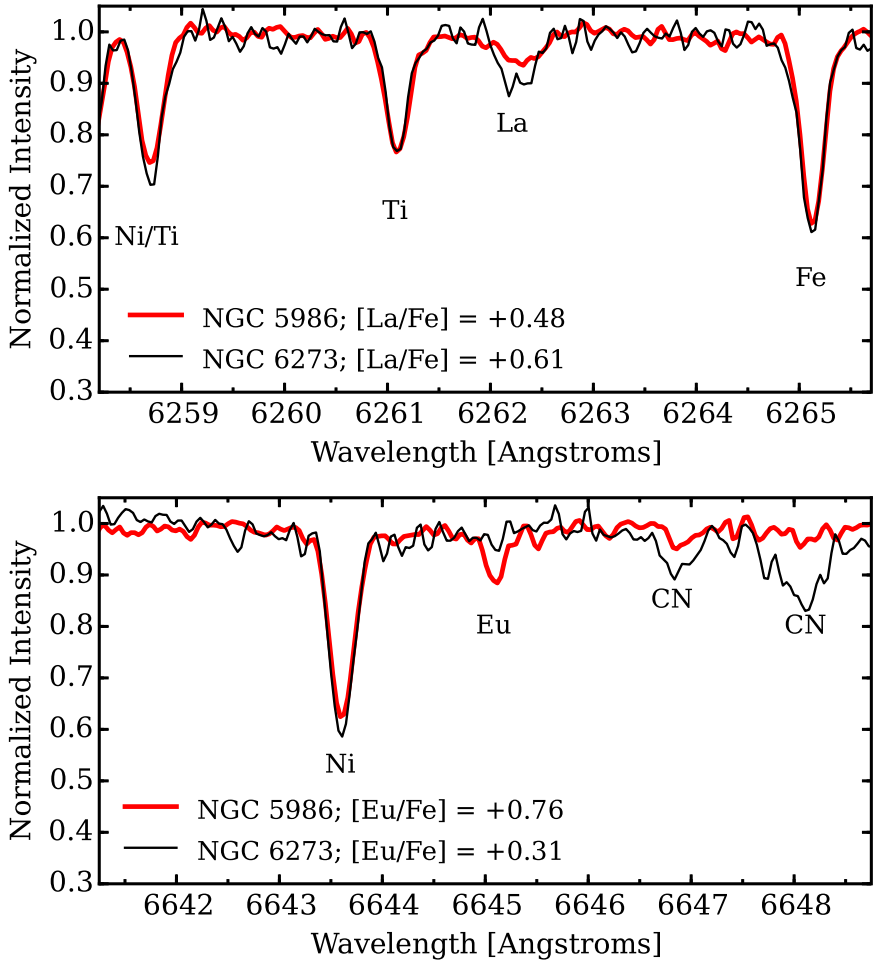

Figure 7. Comparison of the spectra of the NGC 5986 star 2MASS 15460476–3749186 (this work; top panel) and the NGC 6273 star 2MASS 17024412–2616495 (Johnson et al. 2017; bottom panel) for regions near the La II λ6262 and Eu II λ6645 lines. The two stars have similar temperatures, gravities, metallicities, and [La/Fe] abundances but different [Eu/Fe] abundances. Note that the NGC 6273 star exhibits stronger CN lines because it has a different CNO composition.

5986, we find that [Ca/Mg] ranges from −0.17 to +0.33 dex, which is larger than many clusters but less extreme than NGC 2419 and NGC 2808 (e.g., see Carretta 2015, their Figure 14). Therefore, we conclude that the gas from which the second-generation stars in NGC 5986 formed did not experience significant processing at temperatures >100 MK and was instead limited to ∼70–100 MK.

Regardless of the exact pollution source(s), multiple studies agree that dilution/mixing between the ejected material and preexisting gas is likely required to explain the observed abundance patterns (e.g., D'Antona & Ventura 2007; Decressin et al. 2007; D'Ercole et al. 2008; Denissenkov & Hartwick 2014; D'Antona et al. 2016; but see also Bastian et al. 2015). In particular, the shapes of the various light-element anticorrelations in many globular clusters closely resemble simple dilution curves. However, attempts to fit the observed data with simple dilution models have largely failed (Carretta et al. 2012a; Bastian et al. 2015; Carretta 2015; Villanova et al. 2017). In this light, Figure 9 shows the O–Na, Na–Mg, and Mg–Al anticorrelations for NGC 5986 along with dilution curves that represent the expected distributions from mixing first-generation compositions with the most extreme second-generation compositions. Although the O–Na and Na–Mg anticorrelations are nearly aligned with the expected distributions, neither presents an exact match. Compared to the dilution curves, the typical [Na/Fe] abundances of many intermediate-composition stars are systematically too high for a given [O/Fe] or [Mg/Fe] value. Furthermore, the Mg–Al dilution curve is a poor fit to the data. Similar to the cases of NGC 6752 and NGC 2808 (Carretta et al. 2012a; Carretta 2015), we conclude that the light-element distributions in NGC 5986 are not well described by a simple dilution scenario and that more than one significant pollution source must have been present.

5.4. Discrete Populations

In addition to ruling out a simple dilution model, Figures 8–9 indicate that the light-element abundances in NGC 5986 may separate into discrete groups rather than follow a continuous distribution. Using the O–Na panel of Figure 8 and following the nomenclature of Carretta (2014) for NGC 2808, we have identified five possible unique populations in NGC 5986 that are labeled as *P1*, *P2*, *I1*, *I2*, and *E*. In this scheme, the "primordial" *P1* and *P2* groups have higher [O/Fe] and [Mg/Fe] and lower [Na/Fe], [Al/Fe], and [Si/Fe] than the "intermediate" *I1* and *I2* groups, while the "extreme" *E* population (one star) exhibits the lowest [O/Fe] and [Mg/Fe] and highest [Na/Fe], [Al/Fe], and [Si/Fe] abundances. Assuming that each of the identified groups is real, the *P1*, *P2*, *I1*, *I2*, and *E* populations constitute approximately 20%, 40%, 28%, 8%, and 4% of our sample, respectively.

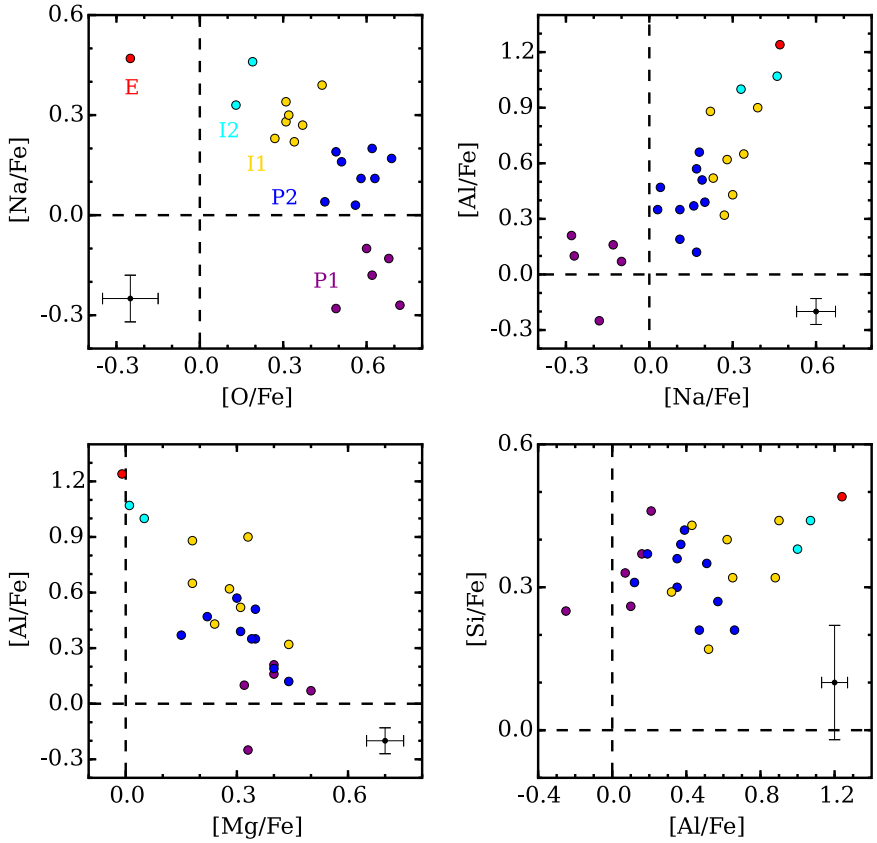

Figure 8. [O/Fe], [Na/Fe], [Mg/Fe], [Al/Fe], and [Si/Fe] plotted against each other to illustrate the O–Na/Mg–Al anticorrelations and Na–Al/Al–Si correlations present in NGC 5986. The [Na/Fe] vs. [O/Fe] plot in particular suggests that approximately five distinct populations with different light-element chemistries may exist. We have labeled and color-coded the "primordial" (*P1*; *P2*), "intermediate" (*I1*; *I2*), and "extreme" (*E*) groups based on the nomenclature used in Carretta (2015) for NGC 2808. The existence of an Al–Si correlation suggests that the gas from which the more Al–rich stars formed was processed at temperatures $\gtrsim$65 MK.

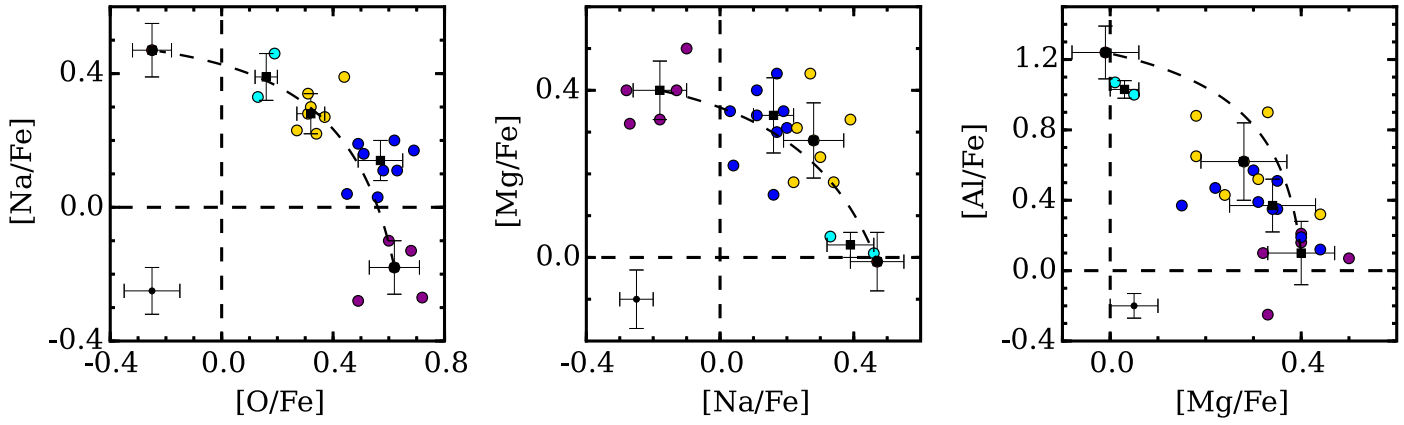

Figure 9. Shape and extent of the O–Na (left), Na–Mg (middle), and Mg–Al (left) anticorrelations present in NGC 5986. The filled black squares indicate the median [X/Fe] ratios for each of the populations identified in Figure 8, and the error bars represent the approximate [X/Fe] dispersion within each population. The dashed black lines are dilution curves, with the end points anchored at the median [X/Fe] values of the *P1* and *E* populations. The remaining symbols are the same as those in Figure 8.

Interestingly, the combined 60% fraction of first-generation composition stars is similar to NGC 2808 (Carretta 2015), which is another cluster known to host at least five populations. Both NGC 2808 and NGC 5986 seem to host anomalously large fractions of first-generation stars.

Although the various populations are relatively well separated in the O–Na panels of Figures 8–9, the composition boundaries distinguishing all five populations are less clear for other elements. Specifically, the Na–Al, Na–Mg, and Mg–Al plots provide strong evidence that at least three discrete populations exist (*P1*, *P2* + *I1*, and *I2* + *E*), but the similar abundance patterns between especially the *P2* and *I1* groups make additional separations more ambiguous. In order to more quantitatively assess the likelihood that at least four to five,

Table 5
Globular Cluster Literature References

Cluster	Source
HP-1	Barbuy et al. (2006)
HP-1	Barbuy et al. (2016)
M10	Haynes et al. (2008)
M107	O'Connell et al. (2011)
M12	Johnson & Pilachowski (2006)
M13	Sneden et al. (2004)
M13	Cohen & Meléndez (2005)
M15	Sneden et al. (1997)
M2	Yong et al. (2014b)
M22	Marino et al. (2011b)
M3	Sneden et al. (2004)
M3	Cohen & Meléndez (2005)
M4	Ivans et al. (1999)
M5	Ivans et al. (2001)
M62	Yong et al. (2014a)
M71	Ramírez & Cohen (2002)
NGC 6342	Johnson et al. (2016)
NGC 6366	Johnson et al. (2016)
NGC 104	Carretta et al. (2004)
NGC 104	Cordero et al. (2014)
NGC 1851	Yong & Grundahl (2008)
NGC 1851	Carretta et al. (2011)
NGC 1851	Gratton et al. (2012b)
NGC 1904	Gratton & Ortolani (1989)
NGC 2419	Cohen & Kirby (2012)
NGC 2808	Carretta et al. (2015)
NGC 288	Shetrone & Keane (2000)
NGC 3201	Gratton & Ortolani (1989)
NGC 362	Shetrone & Keane (2000)
NGC 362	Carretta et al. (2013a)
NGC 4590	Gratton & Ortolani (1989)
NGC 4833	Carretta et al. (2014)
NGC 4833	Roederer & Thompson (2015)
NGC 5286	Marino et al. (2015)
NGC 5824	Roederer et al. (2016)
NGC 5897	Gratton (1987)
NGC 6093	Carretta (2015)
NGC 6273	Johnson et al. (2015b)
NGC 6273	Johnson et al. (2017)
NGC 6287	Lee & Carney (2002)
NGC 6293	Lee & Carney (2002)
NGC 6352	Feltzing et al. (2009)
NGC 6362	Gratton (1987)
NGC 6388	Carretta et al. (2007)
NGC 6397	Gratton & Ortolani (1989)
NGC 6441	Gratton et al. (2006)
NGC 6541	Lee & Carney (2002)
NGC 6752	Yong et al. (2005)

rather than three, unique populations exist, we utilized the Welch's *t*-test to examine differences in the mean light-element [X/Fe], [O/Na], [Na/Mg], [Mg/Al], and [Al/Si] distributions of the *P1*, *P2*, *I1*, and *I2* groups. The *E* population only constitutes one star and is omitted from this analysis; however, since this star has the lowest [O/Fe] and [Mg/Fe] and highest [Na/Fe], [Al/Fe], and [Si/Fe] abundances, we consider the *E* population to be separate from the *I2* stars.

A summary of the Welch *t*-test results is provided in Table 6 and generally reinforces the original hypothesis that up to five populations may exist. If we adopt the common convention that a *p*-value <0.05 indicates that sufficient evidence exists to reject the null hypothesis that two element/population pairs exhibit the same mean composition, then nearly all of the comparisons in Table 6 support more than three populations being present in NGC 5986. A comparison between the *P2* and *I1* groups indicates that the two populations may share similar mean [Mg/Fe] and [Si/Fe] abundances, but the *p*-values for [O/Fe], [Na/Fe], [Al/Fe], [O/Na], and [Na/Mg] are below 0.05. Even though the total sample size is only 25 stars, the *P2* and *I1* groups contain 10 and 7 stars, respectively, and are therefore less sensitive to sampling effects than the other populations. We conclude that the *P2* and *I1* groups are likely distinct populations.

As noted in Section 1, *HST* UV–optical photometry is efficient at separating globular cluster stars with different light-element abundances and provides an alternative method for examining a cluster's light-element composition. In Figure 10, we overlay the locations of the different populations identified here on the $m_{\rm F336W}$ versus $C_{F275W,F336W,F438W}$ pseudo-color–magnitude diagram using data from Piotto et al. (2015) and Soto et al. (2017).[16] Although distinct sequences are not easily separated in Figure 10 from the photometry, perhaps as a result of the moderately high cluster reddening (see Section 4.2), the different populations identified via spectroscopy tend to cluster in distinct regions. For example, the "primordial" stars tend to exhibit the reddest pseudo-colors, while the "intermediate" and "extreme" groups are found at bluer pseudo-colors. Some population mixing is observed in Figure 10, but we suspect that this is largely driven by a combination of reddening and the mixing of RGB and AGB stars in the sample.

Further evidence supporting the existence of discrete populations in NGC 5986 is shown in the right panel of Figure 10, which plots [O/Na] versus [Al/H] (i.e., the elements exhibiting the largest abundance ranges). In general, each group spans a relatively small range in [O/Na] and [Al/H], and the median [O/Na] ratio monotonically decreases as a function of [Al/H]. Additionally, the typical separation in median [O/Na] between adjacent populations is ∼0.35 dex, which is about two times larger than the dispersion within each group (∼0.07 dex, on average). Similarly, the typical separation in median [Al/H] between adjacent groups is ∼0.3 dex, which is about 25% larger than the typical [Al/H] dispersion within each group (∼0.2 dex).

5.5. Comparisons with Similar Clusters

While nearly all monometallic clusters host two to three chemically distinct populations (e.g., Carretta et al. 2009b; Piotto et al. 2015; Milone et al. 2017), those with more than three are relatively rare. Among the monometallic clusters studied in the literature, NGC 2808 is the only convincing case of a cluster hosting at least five populations (Carretta 2015; Milone 2015). The UV–optical color–magnitude diagrams of NGC 5986 are not as complex as those of NGC 2808 (see, e.g., Piotto et al. 2015, their Figures 6 and 10), perhaps because the abundance variations in NGC 5986 are not as extreme, but the data presented in Figures 8–10 support both clusters hosting a similar number of components. An examination of the pseudo-color–magnitude diagram compilations in Piotto et al. (2015) and Milone et al. (2017) suggests that NGC 5986 is actually

[16] The *HST* data are available for download at http://groups.dfa.unipd.it/ESPG/treasury.php. Note that the $C_{F275W,F336W,F438W}$ pseudo-color index is defined as $(m_{F275W}-m_{F336W})-(m_{F336W}-m_{F438W})$.

Table 6
The *t*-statistic, Degrees of Freedom, and *p*-value Results from the Welch's *t*-test

Populations	[O/Fe]	[Na/Fe]	[Mg/Fe]	[Al/Fe]	[Si/Fe]	[O/Na]	[Na/Mg]	[Mg/Al]	[Al/Si]
t (P1−P2)	1.15	−7.98	1.65	−3.54	0.33	6.60	−8.51	3.71	−4.04
dof	8	6	10	7	7	7	12	10	12
p	2.83×10^{-1}	1.52×10^{-4}	1.29×10^{-1}	8.56×10^{-3}	7.48×10^{-1}	2.81×10^{-4}	2.56×10^{-6}	3.96×10^{-3}	1.57×10^{-3}
t (P1−I1)	6.42	−11.27	2.32	−4.86	−0.09	14.85	−11.40	5.20	−5.70
dof	6	7	10	10	9	5	10	10	10
p	5.93×10^{-4}	9.40×10^{-6}	4.31×10^{-2}	7.33×10^{-4}	9.33×10^{-1}	1.69×10^{-5}	5.51×10^{-7}	4.22×10^{-4}	2.10×10^{-4}
t (P1−I2)	9.35	−7.89	9.49	−11.11	−1.56	17.65	−10.51	14.38	−15.77
dof	4	2	5	5	4	4	1	4	4
p	5.45×10^{-4}	2.54×10^{-2}	2.68×10^{-4}	1.10×10^{-4}	1.92×10^{-1}	2.95×10^{-5}	3.53×10^{-2}	7.44×10^{-5}	8.53×10^{-5}
t (P2−I1)	6.53	−5.17	0.83	−2.26	−0.46	11.03	−3.62	2.30	−1.95
dof	12	13	13	11	11	12	13	11	13
p	2.44×10^{-5}	1.71×10^{-4}	4.22×10^{-1}	4.61×10^{-2}	6.54×10^{-1}	1.76×10^{-7}	3.23×10^{-3}	4.22×10^{-2}	7.29×10^{-2}
t (P2−I2)	9.84	−3.82	8.09	−10.18	−2.41	14.62	−6.05	10.77	−8.21
dof	3	1	6	7	2	3	1	5	9
p	1.65×10^{-3}	1.32×10^{-1}	1.47×10^{-4}	2.69×10^{-5}	1.16×10^{-1}	9.79×10^{-4}	6.02×10^{-2}	1.00×10^{-4}	1.68×10^{-5}
t (I1−I2)	4.86	−1.53	6.24	−4.68	−1.53	7.09	−3.77	5.65	−4.36
dof	2	1	6	7	4	2	2	7	6
p	3.62×10^{-2}	3.32×10^{-1}	6.08×10^{-4}	2.26×10^{-3}	1.95×10^{-1}	3.14×10^{-2}	9.43×10^{-2}	9.01×10^{-4}	4.67×10^{-3}

Note. The "E" population is excluded because it consists of only one star.

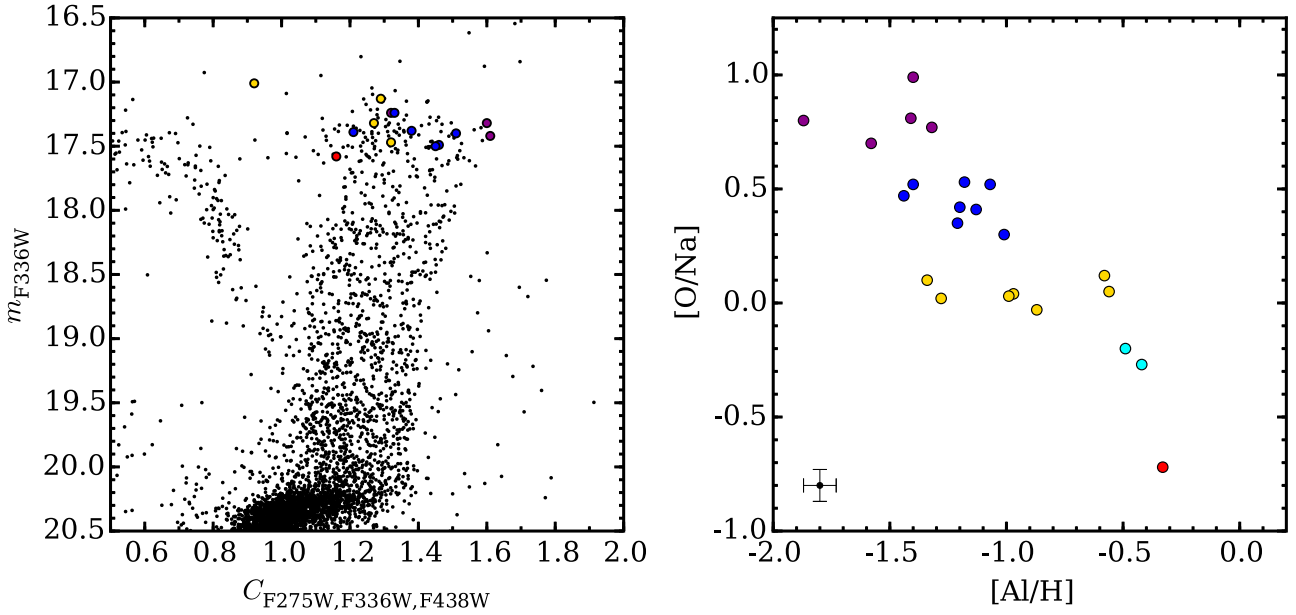

Figure 10. Left: m_{F336W} vs. $C_{F275W,F336W,F438W}$ pseudo-color–magnitude diagram shown for NGC 5986 using data from Piotto et al. (2015) and Soto et al. (2017; small black circles). The large filled circles follow the same color scheme as in Figure 8 and represent overlapping stars between the present study and the *HST* data. In general, stars with lower [O/Fe] and [Mg/Fe] and higher [Na/Fe] and [Al/Fe] exhibit smaller $C_{F275W,F336W,F438W}$ pseudo-color values, but some scatter is present owing to the combined effects of high reddening and the mixing of RGB and AGB stars. Note that the $C_{F275W,F336W,F438W}$ pseudo-color index is defined as $C_{F275W,F336W,F438W} \equiv (m_{F275W}-m_{F336W})-(m_{F336W}-m_{F438W})$ (e.g., Milone et al. 2013). Right: similar to Figure 1 of Gratton et al. (2011), the various stellar populations of NGC 5986 are distinguished using a combination of the measured [O/Na] and [Al/H] ratios. The symbols are the same as those in Figure 8.

very similar to the cluster M13. Furthermore, the pseudo-color–magnitude diagram of NGC 5986 also appears to contain more photometric sequences than the case of NGC 6752, which is confirmed to have at least three distinct populations (Carretta et al. 2012a) and is significantly more complex than a typical cluster like M3.

In Figure 11, we compare histograms of the [O/Na] and [Na/Mg] distributions for NGC 5986 and the similar-metallicity clusters M13, NGC 6752, and M3. Figure 11 reinforces the conclusions from Section 5.4 that NGC 5986 hosts four to five populations, and also shows that the presence of multiple distinct populations can be easily detected in the

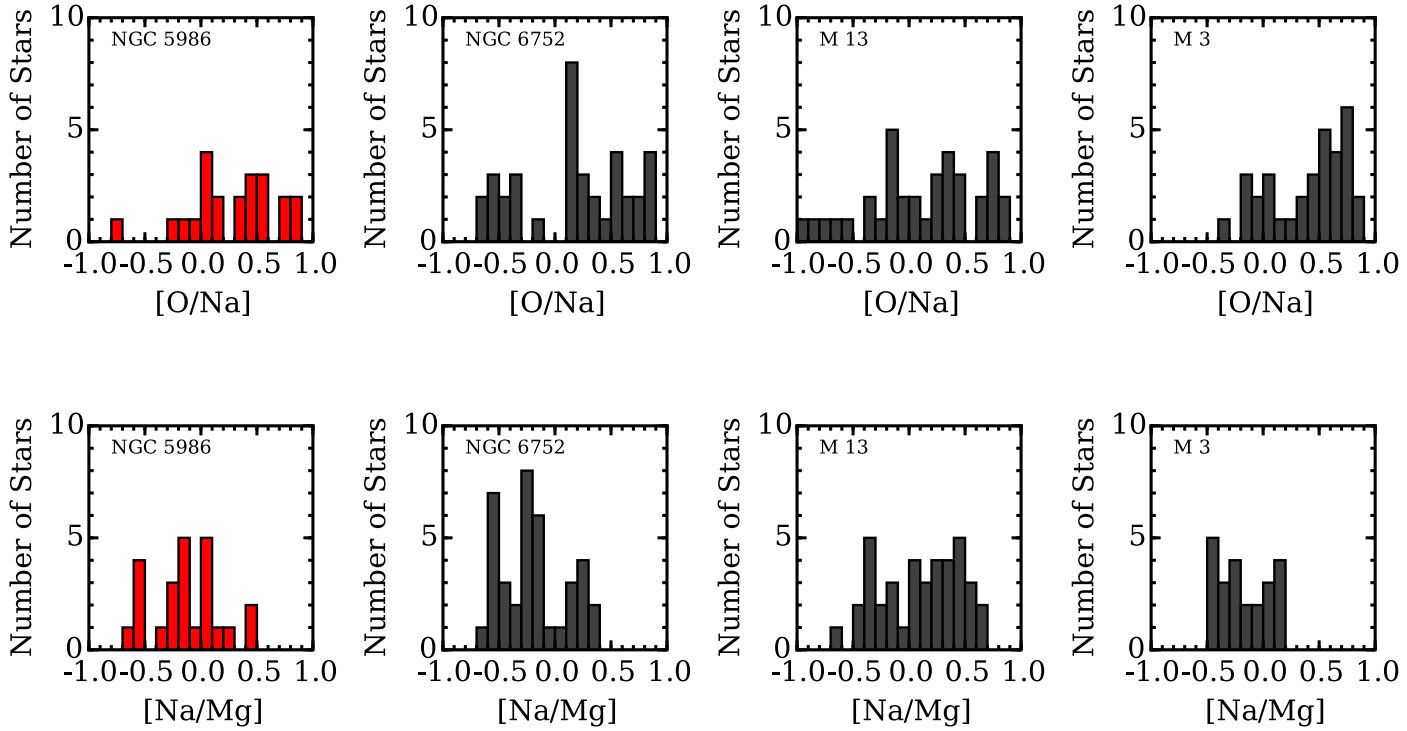

Figure 11. Top: histograms of the [O/Na] distributions for NGC 5986, NGC 6752, M13, and M3, with 0.1 dex bins. Note that all four similar-metallicity clusters exhibit multimodal distributions. Bottom: similar plots illustrating the [Na/Mg] distributions for the same clusters. The data for NGC 6752, M13, and M3 are from Yong et al. (2005), Sneden et al. (2004), and Cohen & Meléndez (2005) and have been shifted to have approximately the same maximum [O/Fe], maximum [Mg/Fe], minimum [Na/Fe], and minimum [Al/Fe] abundances as NGC 5986. The red histograms indicate the data obtained for this paper.

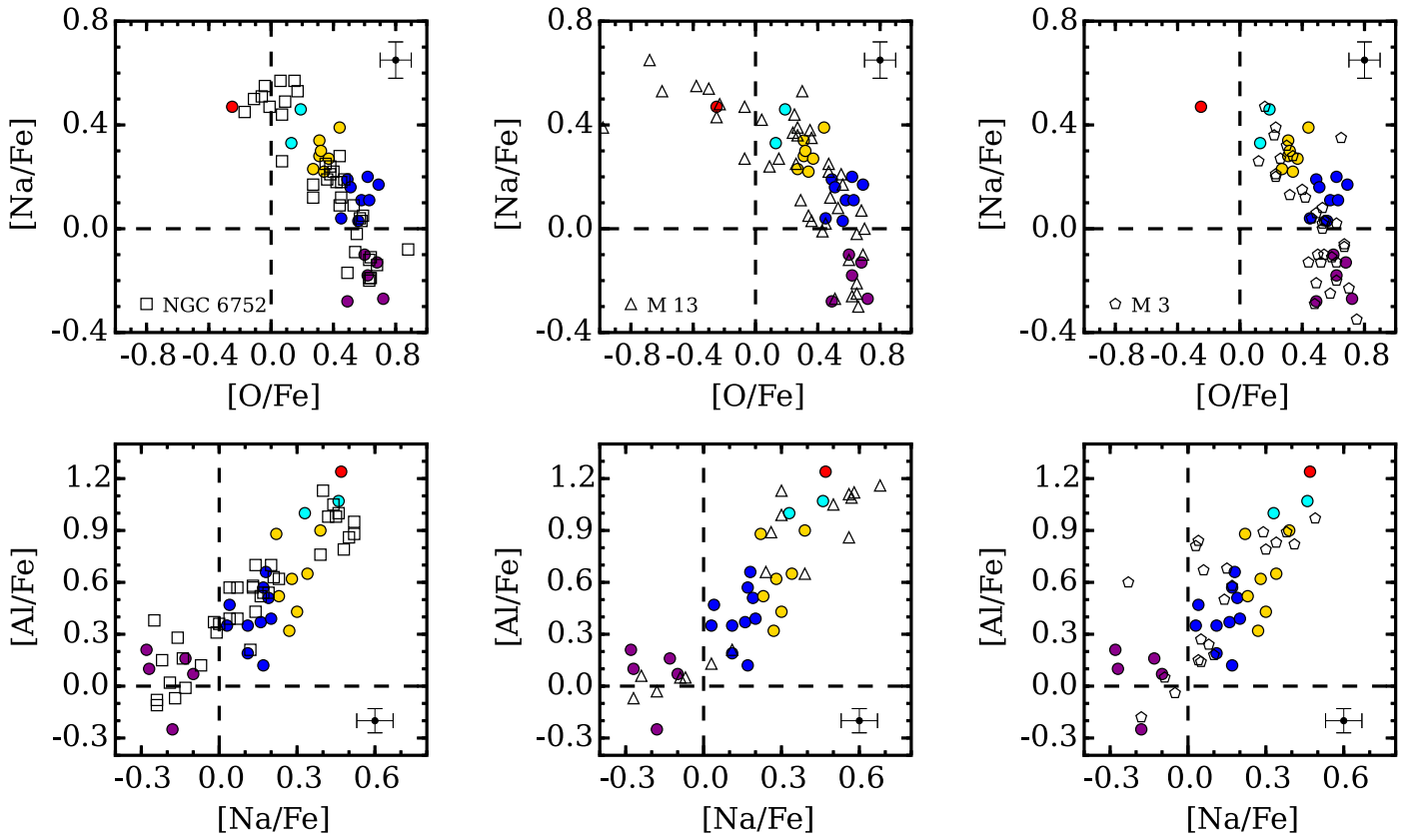

Figure 12. [O/Fe], [Na/Fe], and [Al/Fe] abundance patterns of NGC 5986 (same colored symbols as in Figure 8) compared with those of the similar-metallicity globular clusters NGC 6752 (left; open squares), M13 (middle; open triangles), and M3 (right; open pentagons). The data for NGC 6752, M13, and M3 are from the same sources as in Figure 11. Similarly, the literature data have been shifted to have approximately the same maximum [O/Fe], minimum [Na/Fe], and minimum [Al/Fe] abundances as NGC 5986.

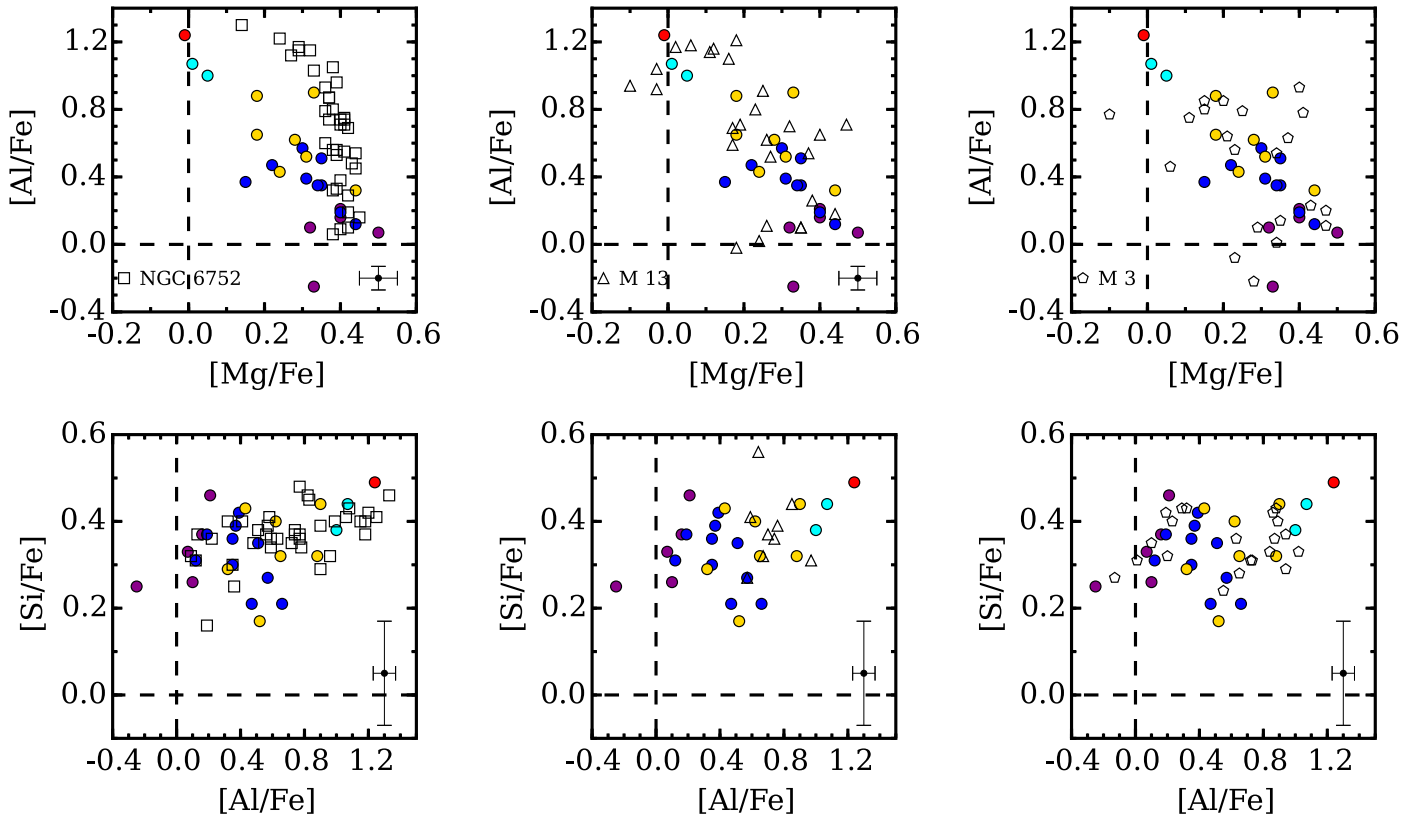

Figure 13. [Mg/Fe], [Al/Fe], and [Si/Fe] abundances of NGC 5986 compared with those of the similar-metallicity globular clusters NGC 6752 (left), M13 (middle), and M3 (right). Similar to Figure 12, the abundances of NGC 6752, M13, and M3 have been shifted to have approximately the same maximum [Mg/Fe], minimum [Al/Fe], and minimum [Si/Fe] abundances as NGC 5986. The colors and symbols are the same as those in Figures 8 and 12.

three other clusters as well. Specifically, Figure 11 indicates that NGC 6752 has at least three populations, M3 has two to three populations, and M13 has four to five populations (see also Monelli et al. 2013).

The similar enrichment histories of NGC 5986 and M13 are further solidified in Figures 12–13, where we directly compare the O–Na, Na–Al, Mg–Al, and Si–Al distributions of all four clusters.[17] Although NGC 5986 and NGC 6752 share similar ranges in [O/Fe], [Na/Fe], [Al/Fe], and [Si/Fe], the full range in [Mg/Fe] is smaller for NGC 6752 and the two clusters exhibit different Mg–Al distributions. Similarly, the *P1*, *P2*, and *I1* populations of NGC 5986 almost identically match the M3 distribution, but M3 does not possess stars matching the *I2* and *E* chemical compositions. In contrast, NGC 5986 and M13 exhibit nearly identical light-element distributions, with the main difference being that the equivalent *E* population in M13 may extend to somewhat lower values of [O/Fe] and higher values of [Na/Fe]. We conclude that NGC 5986 and M13 likely shared similar chemical enrichment histories and were probably enriched by similar classes of polluters.

5.6. Spatial Mixing of First- and Second-generation Stars

A commonly adopted globular cluster formation model posits that stars with compositions similar to the *P1* and *P2* groups in NGC 5986 are the first to form and that these stars are initially distributed at all cluster radii (e.g., D'Ercole et al. 2008). Subsequently, low-velocity gas ejected from sources such as intermediate-mass AGB stars forms a cooling flow that is funneled toward the cluster core, where a second, more centrally concentrated, population forms. As a result, stars with compositions similar to the *I1*, *I2*, and *E* populations of NGC 5986 initially have radial distributions that are distinct from those of first-generation stars. In this model, a cluster's dynamical evolution favors the preferential loss of outer first-generation stars, and remnants of the cluster's initial population gradient may still be observable. However, some simulations indicate that first- and second-generation stars may become spatially mixed after >60% of the initial cluster mass has been lost (e.g., Vesperini et al. 2013; Miholics et al. 2015).

An examination of the radial distributions of first- and second-generation stars in monometallic Galactic globular clusters has produced conflicting results. For example, several earlier papers found that a large fraction of clusters tended to have centrally concentrated second-generation populations (e.g., Carretta et al. 2009b, 2010a; Kravtsov et al. 2011; Lardo et al. 2011; Nataf et al. 2011; Johnson & Pilachowski 2012; Milone et al. 2012b; Richer et al. 2013; Cordero et al. 2014; Massari et al. 2016; Simioni et al. 2016). However, similar studies have also argued either that many clusters have no radial gradient (e.g., Iannicola et al. 2009; Lardo et al. 2011; Milone et al. 2013; Dalessandro et al. 2014; Cordero et al. 2015; Nardiello et al. 2015; Vanderbeke et al. 2015) or that the first-generation stars are actually the most centrally concentrated (e.g., Larsen et al. 2015; Vanderbeke et al. 2015; Lim et al. 2016). Although the measurements are typically straightforward, biases can be introduced because clusters are at different stages in their dynamical evolution and various studies frequently sample different cluster regions.

[17] For Figures 11–13, we have applied systematic offsets to the literature [X/Fe] abundances so that the equivalent *P1* populations of each cluster match the *P1* composition of NGC 5986.

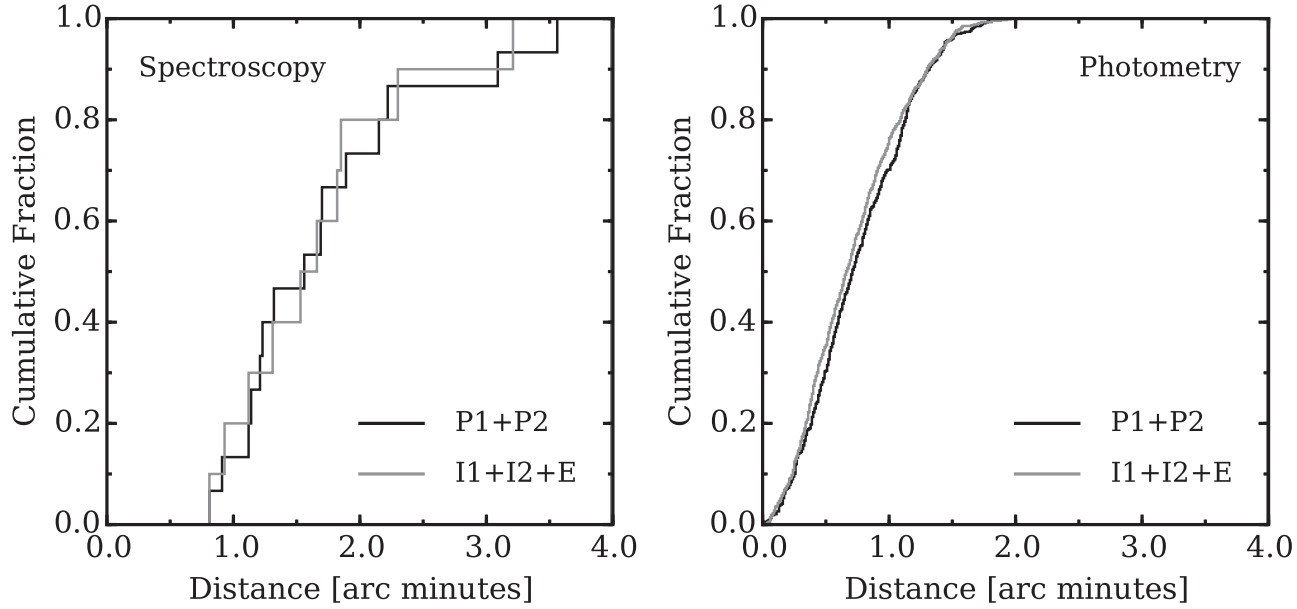

Figure 14. Left: cumulative distribution functions of the *P1* and *P2* populations (black line) and *I1*, *I2*, and *E* populations (gray line), identified via spectroscopy, plotted as a function of the projected radial distance from the cluster center. Right: similar plot indicating the radial distributions of the same populations inferred from the pseudo-colors shown in Figure 9. For the photometric data, we divided the RGB sample in half and assumed that the stars with bluer pseudo-colors are predominantly associated with the *I1*, *I2*, and *E* populations while those with redder pseudo-colors are predominantly associated with the *P1* and *P2* populations. Note that we have adopted a half-mass radius of 0.′98 (Harris 1996) for NGC 5986.

In Figure 14, we show the cumulative radial distributions of the first- (*P1* + *P2*) and second-generation (*I1* + *I2* + *E*) stars measured via spectroscopy and inferred from the *HST* photometry in Figure 10. The advantages of examining both data sets include a substantial increase in the sample size and an extension of the radial coverage from ∼0.8–3.6 half-mass radii[18] to ∼0.01–3.6 half-mass radii. The additional coverage is especially important because models from Vesperini et al. (2013) indicate that the region between ∼1–2 half-mass radii may be where the local ratio of second- to first-generation stars is equivalent to the global ratio.

Interestingly, both the spectroscopic and photometric data in Figure 14 show that the first- and second-generation stars in NGC 5986 share similar radial distributions from the core out to more than 3.5 half-mass radii. Two-sided Kolmogorov–Smirnov tests of the spectroscopic and photometric sets provide *p*-values of 0.999 and 0.175, respectively, which indicate that the data do not provide enough evidence to reject the null hypothesis that the first- and second-generation stars were drawn from the same parent distribution. Therefore, we conclude that the various stellar populations in NGC 5986 are largely spatially mixed over a wide range in cluster radii. If we assume that the first- and second-generation stars were originally segregated but are now spatially mixed, it is possible that the cluster may have lost at least 60%–80% of its original mass (Vesperini et al. 2013; Miholics et al. 2015), perhaps as a consequence of its highly eccentric inner Galaxy orbit (Casetti-Dinescu et al. 2007). However, we caution that the radial distributions may be more nuanced, and it may not necessarily be appropriate to analyze multiple groups (e.g., *I1*, *I2*, and *E*) as a single unit. For example, at least in M13 Johnson & Pilachowski (2012) showed that only the most O-poor stars (*E* group) may be centrally concentrated, and Cordero et al. (2017) further noted that the *E* population exhibits faster rotation than the other subpopulations.

[18] We have adopted 0.′98, the projected half-light radius listed in Harris (1996), as the cluster's half-mass radius. We are assuming that the half-light and half-mass radii are approximately equal.

6. Summary

This paper utilizes high-resolution, high-S/N data from the Magellan-M2FS instrument to obtain radial velocities and chemical abundances for a sample of 43 potential RGB and AGB stars near the Galactic globular cluster NGC 5986. A combination of velocity and [Fe/H] measurements identified 27/43 stars in our sample as likely cluster members, but we were only able to measure detailed abundances for 25/27 member stars. We found NGC 5986 to have a mean heliocentric radial velocity of $+99.76\,\mathrm{km\,s^{-1}}$ ($\sigma = 7.44\,\mathrm{km\,s^{-1}}$) and a mean metallicity of [Fe/H] = −1.54 dex ($\sigma = 0.08$ dex).

The cluster's overall chemical composition characteristics are comparable to other similar-metallicity clusters. For example, the heavier α-elements are uniformly enhanced with $\langle$[Si, Ca/Fe]$\rangle$ = +0.30 dex ($\sigma = 0.08$ dex), and the Fe-peak elements all exhibit nearly solar [X/Fe] ratios. Interestingly, the neutron-capture elements are moderately enhanced with $\langle$[La/Fe]$\rangle$ = +0.42 dex ($\sigma = 0.11$ dex) and $\langle$[Eu/Fe]$\rangle$ = +0.76 dex ($\sigma = 0.08$ dex), and NGC 5986 may be among the most Eu-rich clusters known in the Galaxy. The Eu enhancements are comparable to those found in similar-metallicity stars in several Local Group dwarf galaxies, but NGC 5986 does not share the trait of exhibiting a large [Eu/Fe] dispersion. The cluster's low [La/Eu] ratios, combined with its small [Fe/H] and [La/Eu] dispersions, preclude NGC 5986 from being a member of the iron-complex class, which is characterized by having large dispersions in [La/Eu] that are correlated with metallicity spreads.

We find that NGC 5986 exhibits all of the classical light-element abundance relations, including strong anticorrelations between O–Na, Na–Mg, and Mg–Al and correlations between Na–Al and Al–Si. The combined presence of an Mg–Al anticorrelation and Al–Si correlation suggests that the gas from which the second-generation stars formed must have

experienced burning temperatures of at least 65–70 MK. However, the cluster exhibits neither very low [Mg/Fe] ratios nor a particularly large range in [Ca/Mg] that would indicate significant processing at temperatures exceeding ∼100 MK. The abundance anticorrelations are also not well fit by a simple dilution model, which suggests that more than one class of polluters likely contributed to the cluster's self-enrichment.

One of the most striking results is the discrete nature of the light-element abundance patterns, and we find evidence that NGC 5986 may host at least four to five different populations with distinct compositions. Although the sample sizes within each subpopulation are small, statistical tests support the idea that the commonly observed "primordial" and "intermediate" groups in NGC 5986 may each be further decomposed into populations with distinctly different light-element compositions. Our analysis also identified at least one star that is very O/Mg-poor and Na/Al/Si-rich, which we designated as an "extreme" (*E*) population member. We find that the two primordial (*P1* and *P2*) and intermediate (*I1* and *I2*) groups are present in the proportions 20%, 40%, 28%, and 8%, respectively, while the single *E* population star constitutes the remaining 4% of our sample. If confirmed via photometry and/or larger sample spectroscopic analyses, NGC 5986 would join NGC 2808 as the only known monometallic clusters that host more than three distinct populations. However, we note that a comparison between NGC 5986 and M13 revealed that the two clusters exhibit almost identical composition patterns, and in fact M13 may also be composed of at least four different populations.

Interestingly, an examination of the radial distributions of first- (*P1* and *P2*) and second-generation (*I1*, *I2*, and *E*) stars in NGC 5986 suggests that the populations are well mixed within the cluster. This result is seemingly confirmed from both the spectroscopic sample analyzed here and a photometric sample obtained from the literature. If confirmed, the full spatial mixing of NGC 5986's various populations may suggest either that the stars were never radially segregated or that the cluster may have lost ∼60%–80% of its original mass.

This research has made use of NASA's Astrophysics Data System Bibliographic Services. This publication has made use of data products from the Two Micron All Sky Survey, which is a joint project of the University of Massachusetts and the Infrared Processing and Analysis Center/California Institute of Technology, funded by the National Aeronautics and Space Administration and the National Science Foundation. C.I.J. gratefully acknowledges support from the Clay Fellowship, administered by the Smithsonian Astrophysical Observatory. M.M. is grateful for support from the National Science Foundation to develop M2FS (AST-0923160) and carry out the observations reported here (AST-1312997), and to the University of Michigan for its direct support of M2FS construction and operation. M.G.W. is supported by National Science Foundation grants AST-1313045 and AST-1412999. R.M.R. acknowledges support from grant AST-1413755 from the National Science Foundation. E.W.O. acknowledges support from the National Science Foundation under grant AST-1313006.

References

Allen, C., Moreno, E., & Pichardo, B. 2008, ApJ, 674, 237
Alves, D. R., Bond, H. E., & Onken, C. 2001, AJ, 121, 318
Aoki, W., Honda, S., Sadakane, K., & Arimoto, N. 2007, PASJ, 59, L15
Arnould, M., Goriely, S., & Jorissen, A. 1999, A&A, 347, 572
Barbuy, B., Cantelli, E., Vemado, A., et al. 2016, A&A, 591, A53
Barbuy, B., Zoccali, M., Ortolani, S., et al. 2006, A&A, 449, 349
Barklem, P. S., Christlieb, N., Beers, T. C., et al. 2005, A&A, 439, 129
Bastian, N., Cabrera-Ziri, I., & Salaris, M. 2015, MNRAS, 449, 3333
Bastian, N., & Lardo, C. 2015, MNRAS, 453, 357
Battistini, C., & Bensby, T. 2016, A&A, 586, A49
Bekki, K., & Freeman, K. C. 2003, MNRAS, 346, L11
Bica, E. L. D., & Pastoriza, M. G. 1983, Ap&SS, 91, 99
Bragaglia, A., Carretta, E., Gratton, R., et al. 2010a, A&A, 519, A60
Bragaglia, A., Carretta, E., Gratton, R. G., et al. 2010b, ApJL, 720, L41
Briley, M. M., Hesser, J. E., Bell, R. A., Bolte, M., & Smith, G. H. 1994, AJ, 108, 2183
Briley, M. M., Smith, V. V., Suntzeff, N. B., et al. 1996, Natur, 383, 604
Carretta, E. 2014, ApJL, 795, L28
Carretta, E. 2015, ApJ, 810, 148
Carretta, E., Bragaglia, A., D'Orazi, V., Lucatello, S., & Gratton, R. G. 2010a, A&A, 519, A71
Carretta, E., Bragaglia, A., Gratton, R., & Lucatello, S. 2009a, A&A, 505, 139
Carretta, E., Bragaglia, A., Gratton, R. G., et al. 2007, A&A, 464, 967
Carretta, E., Bragaglia, A., Gratton, R. G., et al. 2009b, A&A, 505, 117
Carretta, E., Bragaglia, A., Gratton, R. G., et al. 2010b, A&A, 516, A55
Carretta, E., Bragaglia, A., Gratton, R. G., et al. 2010c, A&A, 520, A95
Carretta, E., Bragaglia, A., Gratton, R. G., et al. 2013a, A&A, 557, A138
Carretta, E., Bragaglia, A., Gratton, R. G., et al. 2014, A&A, 564, A60
Carretta, E., Bragaglia, A., Gratton, R. G., et al. 2015, A&A, 578, A116
Carretta, E., Bragaglia, A., Gratton, R. G., Lucatello, S., & D'Orazi, V. 2012a, ApJL, 750, L14
Carretta, E., D'Orazi, V., Gratton, R. G., & Lucatello, S. 2012b, A&A, 543, A117
Carretta, E., Gratton, R. G., Bragaglia, A., et al. 2013b, ApJ, 769, 40
Carretta, E., Gratton, R. G., Bragaglia, A., Bonifacio, P., & Pasquini, L. 2004, A&A, 416, 925
Carretta, E., Lucatello, S., Gratton, R. G., Bragaglia, A., & D'Orazi, V. 2011, A&A, 533, A69
Casetti-Dinescu, D. I., Girard, T. M., Herrera, D., et al. 2007, AJ, 134, 195
Castelli, F., & Kurucz, R. L. 2004, arXiv:astro-ph/0405087
Cavallo, R. M., & Nagar, N. M. 2000, AJ, 120, 1364
Cavallo, R. M., Suntzeff, N. B., & Pilachowski, C. A. 2004, AJ, 127, 3411
Cohen, J. G. 1978, ApJ, 223, 487
Cohen, J. G., & Huang, W. 2009, ApJ, 701, 1053
Cohen, J. G., & Huang, W. 2010, ApJ, 719, 931
Cohen, J. G., & Kirby, E. N. 2012, ApJ, 760, 86
Cohen, J. G., & Meléndez, J. 2005, AJ, 129, 303
Cordero, M. J., Hénault-Brunet, V., Pilachowski, C. A., et al. 2017, MNRAS, 465, 3515
Cordero, M. J., Pilachowski, C. A., Johnson, C. I., et al. 2014, ApJ, 780, 94
Cordero, M. J., Pilachowski, C. A., Johnson, C. I., & Vesperini, E. 2015, ApJ, 800, 3
da Costa, G. S. 2016, in IAU Symp. 317, The General Assembly of Galaxy Halos: Structure, Origin and Evolution, ed. A. Bragalia et al. (Cambridge: Cambridge Univ. Press), 110
Da Costa, G. S., Norris, J. E., & Yong, D. 2013, ApJ, 769, 8
Dalessandro, E., Lapenna, E., Mucciarelli, A., et al. 2016, ApJ, 829, 77
Dalessandro, E., Massari, D., Bellazzini, M., et al. 2014, ApJL, 791, L4
D'Antona, F., & Ventura, P. 2007, MNRAS, 379, 1431
D'Antona, F., Vesperini, E., D'Ercole, A., et al. 2016, MNRAS, 458, 2122
D'Ercole, A., Vesperini, E., D'Antona, F., McMillan, S. L. W., & Recchi, S. 2008, MNRAS, 391, 825
D'Orazi, V., Lucatello, S., Gratton, R., et al. 2010, ApJL, 713, L1
de Mink, S. E., Pols, O. R., Langer, N., & Izzard, R. G. 2009, A&A, 507, L1
Decressin, T., Meynet, G., Charbonnel, C., Prantzos, N., & Ekström, S. 2007, A&A, 464, 1029
Denisenkov, P. A., & Denisenkova, S. N. 1990, SvAL, 16, 275
Denissenkov, P. A., & Hartwick, F. D. A. 2014, MNRAS, 437, L21
Dobrovolskas, V., Kučinskas, A., Bonifacio, P., et al. 2014, A&A, 565, A121
Doherty, C. L., Gil-Pons, P., Lau, H. H. B., et al. 2014, MNRAS, 441, 582
Dotter, A., Sarajedini, A., Anderson, J., et al. 2010, ApJ, 708, 698
Drake, J. J., Smith, V. V., & Suntzeff, N. B. 1992, ApJL, 395, L95
Dupree, A. K., Avrett, E. H., & Kurucz, R. L. 2016, ApJL, 821, L7
Dupree, A. K., Strader, J., & Smith, G. H. 2011, ApJ, 728, 155
Feltzing, S., Primas, F., & Johnson, R. A. 2009, A&A, 493, 913
Geisler, D., Claria, J. J., & Minniti, D. 1997, PASP, 109, 799
Georgiev, I. Y., Hilker, M., Puzia, T. H., Goudfrooij, P., & Baumgardt, H. 2009, MNRAS, 396, 1075

Gratton, R., Sneden, C., & Carretta, E. 2004, ARA&A, 42, 385
Gratton, R. G. 1987, A&A, 179, 181
Gratton, R. G., Bonifacio, P., Bragaglia, A., et al. 2001, A&A, 369, 87
Gratton, R. G., Carretta, E., & Bragaglia, A. 2012a, A&ARv, 20, 50
Gratton, R. G., Johnson, C. I., Lucatello, S., D'Orazi, V., & Pilachowski, C. 2011, A&A, 534, A72
Gratton, R. G., Lucatello, S., Bragaglia, A., et al. 2006, A&A, 455, 271
Gratton, R. G., Lucatello, S., Carretta, E., et al. 2012b, A&A, 539, A19
Gratton, R. G., & Ortolani, S. 1989, A&A, 211, 41
Hansen, T. T., Simon, J. D., Marshall, J. L., et al. 2017, ApJ, 838, 44
Harris, W. E. 1996, AJ, 112, 1487
Hatzes, A. P. 1987, PASP, 99, 369
Haynes, S., Burks, G., Johnson, C. I., & Pilachowski, C. A. 2008, PASP, 120, 1097
Hesser, J. E., Shawl, S. J., & Meyer, J. E. 1986, PASP, 98, 403
Hollyhead, K., Kacharov, N., Lardo, C., et al. 2017, MNRAS, 465, L39
Iannicola, G., Monelli, M., Bono, G., et al. 2009, ApJL, 696, L120
Ivans, I. I., Kraft, R. P., Sneden, C., et al. 2001, AJ, 122, 1438
Ivans, I. I., Sneden, C., Kraft, R. P., et al. 1999, AJ, 118, 1273
Izzard, R. G., Lugaro, M., Karakas, A. I., Iliadis, C., & van Raai, M. 2007, A&A, 466, 641
Jasniewicz, G., de Laverny, P., Parthasarathy, M., Lèbre, A., & Thévenin, F. 2004, A&A, 423, 353
Ji, A. P., Frebel, A., Simon, J. D., & Chiti, A. 2016, ApJ, 830, 93
Johnson, C. I., Caldwell, N., Rich, R. M., et al. 2017, ApJ, 836, 168
Johnson, C. I., Caldwell, N., Rich, R. M., Pilachowski, C. A., & Hsyu, T. 2016, AJ, 152, 21
Johnson, C. I., Kraft, R. P., Pilachowski, C. A., et al. 2005, PASP, 117, 1308
Johnson, C. I., McDonald, I., Pilachowski, C. A., et al. 2015a, AJ, 149, 71
Johnson, C. I., McWilliam, A., & Rich, R. M. 2013, ApJL, 775, L27
Johnson, C. I., & Pilachowski, C. A. 2006, AJ, 132, 2346
Johnson, C. I., & Pilachowski, C. A. 2010, ApJ, 722, 1373
Johnson, C. I., & Pilachowski, C. A. 2012, ApJL, 754, L38
Johnson, C. I., Rich, R. M., Kobayashi, C., & Fulbright, J. P. 2012, ApJ, 749, 175
Johnson, C. I., Rich, R. M., Kobayashi, C., Kunder, A., & Koch, A. 2014, AJ, 148, 67
Johnson, C. I., Rich, R. M., Pilachowski, C. A., et al. 2015b, AJ, 150, 63
Kraft, R. P. 1994, PASP, 106, 553
Kraft, R. P., & Ivans, I. I. 2003, PASP, 115, 143
Kraft, R. P., Sneden, C., Langer, G. E., & Shetrone, M. D. 1993, AJ, 106, 1490
Kraft, R. P., Sneden, C., Smith, G. H., et al. 1997, AJ, 113, 279
Kravtsov, V., Alcaíno, G., Marconi, G., & Alvarado, F. 2011, A&A, 527, L9
Kravtsov, V. V., Pavlov, M. V., Samus', N. N., et al. 1997, AstL, 23, 391
Kurtz, M. J., & Mink, D. J. 1998, PASP, 110, 934
Langer, G. E., Hoffman, R., & Sneden, C. 1993, PASP, 105, 301
Langer, G. E., Hoffman, R. E., & Zaidins, C. S. 1997, PASP, 109, 244
Lardo, C., Bellazzini, M., Pancino, E., et al. 2011, A&A, 525, A114
Lardo, C., Mucciarelli, A., & Bastian, N. 2016, MNRAS, 457, 51
Larsen, S. S., Baumgardt, H., Bastian, N., et al. 2015, ApJ, 804, 71
Larsen, S. S., Brodie, J. P., Grundahl, F., & Strader, J. 2014, ApJ, 797, 15
Lawler, J. E., Bonvallet, G., & Sneden, C. 2001a, ApJ, 556, 452
Lawler, J. E., Wickliffe, M. E., den Hartog, E. A., & Sneden, C. 2001b, ApJ, 563, 1075
Lee, J.-W. 2016, ApJS, 226, 16
Lee, J.-W., & Carney, B. W. 2002, AJ, 124, 1511
Lee, Y.-W., Gim, H. B., & Casetti-Dinescu, D. I. 2007, ApJL, 661, L49
Lemasle, B., de Boer, T. J. L., Hill, V., et al. 2014, A&A, 572, A88
Letarte, B., Hill, V., Tolstoy, E., et al. 2010, A&A, 523, A17
Lim, D., Lee, Y.-W., Pasquato, M., Han, S.-I., & Roh, D.-G. 2016, ApJ, 832, 99
Marino, A. F., Milone, A. P., Karakas, A. I., et al. 2015, MNRAS, 450, 815
Marino, A. F., Milone, A. P., Piotto, G., et al. 2009, A&A, 505, 1099
Marino, A. F., Milone, A. P., Piotto, G., et al. 2011a, ApJ, 731, 64
Marino, A. F., Sneden, C., Kraft, R. P., et al. 2011b, A&A, 532, A8
Massari, D., Lapenna, E., Bragaglia, A., et al. 2016, MNRAS, 458, 4162
Mateo, M., Bailey, J. I., Crane, J., et al. 2012, Proc. SPIE, 8446, 84464Y
McWilliam, A., Fulbright, J., & Rich, R. M. 2010, in IAU Symp. 265, Chemical Abundances in the Universe: Connecting First Stars to Planets, ed. K. Cunha, M. Spite, & B. Barbuy (Cambridge: Cambridge Univ. Press), 279
Mészáros, S., Martell, S. L., Shetrone, M., et al. 2015, AJ, 149, 153
Miholics, M., Webb, J. J., & Sills, A. 2015, MNRAS, 454, 2166
Milone, A. P. 2015, MNRAS, 446, 1672
Milone, A. P., Marino, A. F., Piotto, G., et al. 2012a, ApJ, 745, 27
Milone, A. P., Marino, A. F., Piotto, G., et al. 2013, ApJ, 767, 120
Milone, A. P., Marino, A. F., Piotto, G., et al. 2015a, ApJ, 808, 51
Milone, A. P., Marino, A. F., Piotto, G., et al. 2015b, MNRAS, 447, 927
Milone, A. P., Piotto, G., Bedin, L. R., et al. 2012b, ApJ, 744, 58
Milone, A. P., Piotto, G., Renzini, A., et al. 2017, MNRAS, 464, 3636
Momany, Y., Bedin, L. R., Cassisi, S., et al. 2004, A&A, 420, 605
Monelli, M., Milone, A. P., Stetson, P. B., et al. 2013, MNRAS, 431, 2126
Moni Bidin, C., Moehler, S., Piotto, G., Momany, Y., & Recio-Blanco, A. 2009, A&A, 498, 737
Moreno, E., Pichardo, B., & Velázquez, H. 2014, ApJ, 793, 110
Mottini, M., Wallerstein, G., & McWilliam, A. 2008, AJ, 136, 614
Mucciarelli, A., Bellazzini, M., Ibata, R., et al. 2012, MNRAS, 426, 2889
Mucciarelli, A., Bellazzini, M., Merle, T., et al. 2015a, ApJ, 801, 68
Mucciarelli, A., Lapenna, E., Massari, D., et al. 2015b, ApJ, 809, 128
Mucciarelli, A., Lapenna, E., Massari, D., Ferraro, F. R., & Lanzoni, B. 2015c, ApJ, 801, 69
Mucciarelli, A., Origlia, L., Ferraro, F. R., & Pancino, E. 2009, ApJL, 695, L134
Nardiello, D., Milone, A. P., Piotto, G., et al. 2015, A&A, 573, A70
Nataf, D. M., Gould, A., Pinsonneault, M. H., & Stetson, P. B. 2011, ApJ, 736, 94
Niederhofer, F., Bastian, N., Kozhurina-Platais, V., et al. 2017, MNRAS, 465, 4159
Norris, J., Cottrell, P. L., Freeman, K. C., & Da Costa, G. S. 1981, ApJ, 244, 205
Norris, J., & Pilachowski, C. A. 1985, ApJ, 299, 295
Norris, J. E. 2004, ApJL, 612, L25
Norris, J. E., & Da Costa, G. S. 1995, ApJ, 447, 680
O'Connell, J. E., Johnson, C. I., Pilachowski, C. A., & Burks, G. 2011, PASP, 123, 1139
Ortolani, S., Momany, Y., Barbuy, B., Bica, E., & Catelan, M. 2000, A&A, 362, 953
Pasquini, L., Mauas, P., Käufl, H. U., & Cacciari, C. 2011, A&A, 531, A35
Peterson, R. C. 1980, ApJL, 237, L87
Pilachowski, C. A., Sneden, C., Kraft, R. P., & Langer, G. E. 1996, AJ, 112, 545
Piotto, G., Bedin, L. R., Anderson, J., et al. 2007, ApJL, 661, L53
Piotto, G., Milone, A. P., Anderson, J., et al. 2012, ApJ, 760, 39
Piotto, G., Milone, A. P., Bedin, L. R., et al. 2015, AJ, 149, 91
Piotto, G., Villanova, S., Bedin, L. R., et al. 2005, ApJ, 621, 777
Prantzos, N., Charbonnel, C., & Iliadis, C. 2007, A&A, 470, 179
Rakos, K., & Schombert, J. 2005, PASP, 117, 245
Ramírez, S. V., & Cohen, J. G. 2002, AJ, 123, 3277
Recio-Blanco, A., Piotto, G., de Angeli, F., et al. 2005, A&A, 432, 851
Renzini, A. 2008, MNRAS, 391, 354
Renzini, A., D'Antona, F., Cassisi, S., et al. 2015, MNRAS, 454, 4197
Richer, H. B., Heyl, J., Anderson, J., et al. 2013, ApJL, 771, L15
Roederer, I. U. 2011, ApJL, 732, L17
Roederer, I. U., Mateo, M., Bailey, J. I., et al. 2016, MNRAS, 455, 2417
Roederer, I. U., Preston, G. W., Thompson, I. B., et al. 2014, AJ, 147, 136
Roederer, I. U., & Thompson, I. B. 2015, MNRAS, 449, 3889
Rosenberg, A., Piotto, G., Saviane, I., & Aparicio, A. 2000, A&AS, 144, 5
Rutledge, G. A., Hesser, J. E., Stetson, P. B., et al. 1997, PASP, 109, 883
Sbordone, L., Monaco, L., Moni Bidin, C., et al. 2015, A&A, 579, A104
Schiavon, R. P., Caldwell, N., Conroy, C., et al. 2013, ApJL, 776, L7
Shetrone, M., Venn, K. A., Tolstoy, E., et al. 2003, AJ, 125, 684
Shetrone, M. D., Côté, P., & Sargent, W. L. W. 2001, ApJ, 548, 592
Shetrone, M. D., & Keane, M. J. 2000, AJ, 119, 840
Simioni, M., Milone, A. P., Bedin, L. R., et al. 2016, MNRAS, 463, 449
Skrutskie, M. F., Cutri, R. M., Stiening, R., et al. 2006, AJ, 131, 1163
Smith, V. V., Suntzeff, N. B., Cunha, K., et al. 2000, AJ, 119, 1239
Sneden, C. 1973, ApJ, 184, 839
Sneden, C., Kraft, R. P., Guhathakurta, P., Peterson, R. C., & Fulbright, J. P. 2004, AJ, 127, 2162
Sneden, C., Kraft, R. P., Shetrone, M. D., et al. 1997, AJ, 114, 1964
Sneden, C., Lucatello, S., Ram, R. S., Brooke, J. S. A., & Bernath, P. 2014, ApJS, 214, 26
Sneden, C., Pilachowski, C. A., & Kraft, R. P. 2000, AJ, 120, 1351
Sobeck, J. S., Kraft, R. P., Sneden, C., et al. 2011, AJ, 141, 175
Soto, M., Bellini, A., Anderson, J., et al. 2017, AJ, 153, 19
Valcarce, A. A. R., & Catelan, M. 2011, A&A, 533, A120
Van der Swaelmen, M., Barbuy, B., Hill, V., et al. 2016, A&A, 586, A1
Vanderbeke, J., De Propris, R., De Rijcke, S., et al. 2015, MNRAS, 451, 275
Ventura, P., & D'Antona, F. 2009, A&A, 499, 835
Ventura, P., D'Antona, F., Di Criscienzo, M., et al. 2012, ApJL, 761, L30
Ventura, P., García-Hernández, D. A., Dell'Agli, F., et al. 2016, ApJL, 831, L17

Vesperini, E., McMillan, S. L. W., D'Antona, F., & D'Ercole, A. 2013, MNRAS, 429, 1913
Villanova, S., Geisler, D., Piotto, G., & Gratton, R. G. 2012, ApJ, 748, 62
Villanova, S., Moni Bidin, C., Mauro, F., Munoz, C., & Monaco, L. 2017, MNRAS, 464, 2730
Yong, D., Alves Brito, A., Da Costa, G. S., et al. 2014a, MNRAS, 439, 2638
Yong, D., & Grundahl, F. 2008, ApJL, 672, L29
Yong, D., Grundahl, F., Nissen, P. E., Jensen, H. R., & Lambert, D. L. 2005, A&A, 438, 875
Yong, D., Roederer, I. U., Grundahl, F., et al. 2014b, MNRAS, 441, 3396
Zinn, R. 1980, ApJS, 42, 19
Zinn, R., & West, M. J. 1984, ApJS, 55, 45